Universidade de Lisboa
Faculdade de Ciências
Departamento de Física

Self-Assembly of Colloids Driven by External Fields

André S. Nunes

Orientadores:

Nuno Araújo e Margarida Telo da Gama

Dissertação
Mestrado em Física
Especialização em Física Estatística e Não-Linear

2015

Abstract

We study self-assembly of colloidal particles under the influence of two types of external fields: one space-dependent where the system evolves into a stationary state (equilibrium) and the other time-dependent that keeps the system out of equilibrium at all times. We perform extensive Brownian dynamics simulations with different field profiles. In the first case, we analyze the formation of bands of colloidal particles driven by periodic external fields. We determine the dependence of the band width on the strength of the particle/particle interaction and on the strength and periodicity of the field. We also investigate the switching (field-on) dynamics and the relaxation times as a function of the system parameters. The observed scaling relations were analyzed using a simple dynamic density-functional theory of fluids. In the second case, we study the formation and stability of lanes under the influence of time-varying (rotating) fields. Lanes are stable kinetic structures formed in colloidal mixtures composed by opposite charged particles subjected to counterflow imposed by a uniform external field. We find that these structures resist the rotation of the field for small angles (increasing the shift between the lanes orientation and the direction of the field) but they are destroyed and rearranged into lanes along new orientations according to quantized angles (the magic angles) in a system with periodic boundary conditions. The evolution is constrained by these magic angles and has a dependence on the angular velocity of the field and its intensity. We also employ the Voronoi tessellation method to identify the clusters during the evolution and find that both the number of clusters and the distribution of the area of the Voronoi cells depend on the state of the system. When the evolution is trapped in a lane configuration the number of clusters is minimal and there is a greater number of small cells compared with the mixed state in which particles move along the field direction.

KEYWORDS:

Colloids, Brownian dynamics, systems far from equilibrium, relaxation towards equilibrium.

Resumo

A possibilidade de fabrico de materiais com propriedades físicas melhoradas através da auto-organização de partículas coloidais tem motivado estudos teóricos e experimentais ao longo das décadas. Inicialmente, o foco era a identificação de novas fases e a construção de diagramas de fase em equilíbrio, com base nas propriedades individuais das partículas, tais como a forma, o tamanho e a química. Contudo, o avanço de técnicas óticas e litográficas abriu a possibilidade de explorar outras alternativas, por exemplo, o uso de substratos e interfaces, o controlo do meio de suspensão ou a agregação sob o efeito de um fluxo. Mais recentemente, tem vindo a haver um crescente interesse na auto-organização na presença de campos eletromagnéticos (EM).

Campos EM uniformes conjugados com os graus de liberdade rotacionais de partículas magnéticas não-esféricas permitem o controlo da sua orientação ou ajustar a intensidade e direção das interações das partículas. Campos que variam no espaço são usados para restringir a posição das partículas, formando moldes virtuais que induzem padrões periódicos no espaço.

Sob a influência de constrangimentos externos, as suspensões coloidais são habitualmente levadas para fora do equilíbrio e a relaxação para o novo equilíbrio resulta da competição entre vários mecanismos que ocorrem a diferentes escalas espaciais e temporais. Como tal, para além da identificação das estruturas de equilíbrio e da sua dependência das condições experimentais, é extremamente interessante do ponto de vista prático caracterizar os percursos cinéticos que levam à formação das estruturas de interesse e das escalas de tempo envolvidas.

Parte desta tese é centrada no estudo de um caso protótipo de auto-organização guiada por um campo externo. Para simplificar, consideramos a formação de bandas induzida por um campo EM sinusoidal e estudamos como as estruturas de equilíbrio e a dinâmica para o equilíbrio dependem da magnitude e periodicidade do campo, assim como da interação entre partículas. Os resultados das simulações do sistema feitas com o método da dinâmica Browniana são comparados com uma análise contínua baseada na teoria dinâmica da densidade funcional dos fluidos (DDFT).

Estabelecemos uma excelente concordância qualitativa entre os resultados numéricos e analíticos do comportamento do perfil de densidade de partículas quando sujeito a alterações nos parâmetros do campo externo. A análise em equilíbrio é feita com base na espessura das bandas. Observamos que a largura aumenta com a intensidade da interação partícula/partícula e diminui com a intensidade do campo externo e determinámos as dependências. Estes dois mecanismos têm influências contrárias na formação de estruturas em equilíbrio. Descobrimos também que existe uma relação direta entre a largura das bandas e o número de bandas no sistema, sendo possível re-escalar a primeira em função da segunda.

Fizemos também o estudo dos tempos de relaxação do sistema até chegar ao equilíbrio. Mais uma vez os resultados numéricos e teóricos são bastante consistentes. Os tempos de relaxação dependem da posição sendo mais curtos para as regiões em que a densidade é mais baixa no equilíbrio. Determinámos que a dinâmica do perfil de densidades é exponencial nos pontos de densidade máxima e mínima. Os parâmetros do campo externo e da interação entre partículas também têm uma influência nos tempos de relaxação. Nos pontos de densidade máxima, o aumento das intensidades do campo e das interações partícula/partícula aceleram a dinâmica enquanto nos pontos de densidade mínima a dependência é mais complexa e existe um tempo de relaxação máximo que depende das intensidades do campo e das interações partícula/partícula. Também os tempos de relaxação podem ser re-escalados pelo número de bandas.

Vários padrões não triviais surgem em sistemas constituídos por muitas partículas que se encontram longe do equilíbrio. A física fora de equilíbrio é uma área em intensa proliferação que introduz novos desafios do ponto de vista do desenvolvimento de ferramentas de estudo, que são bastante distintas daquelas utilizadas para o equilíbrio. As propriedades destes sistemas têm dependências temporais que tornam a sua análise mais complexa. Os coloides são excelentes para estudar estes sistemas, uma vez que experimentalmente é possível observar a posição (e trajetória individual) das partículas recorrendo a técnicas óticas convencionais.

Noutra parte da tese, focamo-nos na dinâmica guiada por um campo externo rotativo que varia no tempo. Campos magnéticos rotativos podem ser usados para auto-organizar partículas coloidais com dipolos magnéticos permanentes. Aplicámos a dinâmica Browniana para estudar a resistência da estrutura das faixas à rotação do campo. Estas faixas são observadas experimentalmente em plasmas complexos, tráfico de pedestres e misturas coloidais. Elas são formadas espontaneamente em sistemas com um campo uniforme para reduzir as colisões frontais entre partículas com cargas opostas. Esta é considerada uma transição de fase fora do equilíbrio que é causada pelo balanço entre a intensidade da interação partícula/partícula e a intensidade do campo externo. São formadas apenas acima de um valor crítico da intensidade do campo. A densidade do número de partículas no sistema também desempenha um papel importante. Para densidades baixas, não há colisões suficientes para se observar a transição, para densidades elevadas o sistema fica bloqueado e as partículas não se movimentam. Apenas em valores intermédios são observadas a estrutura das faixas. Estas estruturas correspondem às configurações iniciais nas simulações.

Descobrimos que as faixas formam obstáculos à passagem de partículas com carga oposta que querem mover-se de acordo com a direção do campo externo, o que resulta na resistência destas estruturas a pequenas rotações do campo. Contudo, as interfaces que se criam entre faixas de carga oposta não conseguem resistir à alteração constante na direção do campo externo e são eventualmente destruídas. O sistema atravessa um estado de desordem mas a estrutura das faixas produz-se novamente segundo uma nova orientação, mais próxima da direção do campo. Num sistema com condições fronteira periódicas as faixas reorganizam-se segundo ângulos (ângulos mágicos) que estão quantizados e são definidos pela geometria do sistema. O ângulo mágico adotado pelas faixas corresponde àquele mais próximo da direção do campo externo no momento da reestruturação.

Estudámos também a influência da velocidade angular e da intensidade do campo externo na dinâmica do sistema. Para velocidades angulares baixas, a orientação das faixas e o tempo aproximado de formação podem ser determinados pelos parâmetros do campo. Neste regime existe uma grande consistência entre a evolução de diferentes amostras e elas tornam-se periódicas, com o período dos ângulos mágicos. As condições iniciais só afetam o primeiro período, após o qual o sistema entra num estado estacionário. Para velocidades angulares elevadas, o comportamento não é tão simples. A formação e destruição de faixas tornam-se irregulares mas a sua orientação continua a seguir os ângulos mágicos. Concluímos também que aumentando a velocidade angular o sistema passa mais tempo no estado misturado em que não existem faixas.

Usámos ainda o método de tecelagem de Voronoi para a análise deste sistema. Isto permite-nos fazer a lista de primeiros vizinhos de cada partícula, traçar a célula que limita a região de pontos que se encontram mais próximos de cada partícula e identificar os agregados em cada momento. Este método confirma que em momentos de reestruturação o número de agregados é elevado e oscila rapidamente, enquanto que quando há faixas formadas o número de agregados é reduzido. A área das células de Voronoi para cada partícula está relacionada com a distância aos vizinhos mais próximos, e portanto, com a densidade na região em que a partícula se encontra. Nos momentos em que o sistema está organizado em faixas existe um maior número de células cuja área é baixa do que quando o sistema está misturado, uma evidência da compressão de partículas nas interfaces.

PALAVRAS-CHAVE:

Colloides, dinâmica Browniana, sistemas fora de equilíbrio, relaxação para o equilíbrio.

Acknowledgements

I would like to thank my supervisors Nuno Araújo and Margarida Telo da Gama for their energetic guidance and for introducing me to this very interesting subject.

I also acknowledge fruitful discussions with Daniel de las Heras, Cristovão Dias, José S. Andrade Jr. and Robert Ziff that helped to significantly improve the contents of this thesis, as well as financial support from the Portuguese Foundation for Science and Technology (FCT) under Contracts nos. IF/00255/2013, EXCL/FIS-NAN/0083/2012 and UID/FIS/00618/2013.

Contents

Chapter 1

Introduction

The possibility of obtaining materials with enhanced physical properties from the self-assembly of colloidal particles has motivated experimental and theoretical studies over decades [1–4]. Initially, the focus was on identifying novel phases and constructing the equilibrium phase diagrams, based on the properties of the individual particles (shape, size, and chemistry) [5–8]. However, the impressive advance of optical and lithographic techniques opened the possibility of exploring alternative routes as, for example, the use of substrates and interfaces [9–14], the control of the suspending medium [15] or the assembly under flow [16]. More recently, there has been a sustained interest on the self-assembly under the presence of an electromagnetic (EM) field [17–21]. Uniform EM fields couple to the rotational degrees of freedom of magnetic aspherical particles allow to control their orientation [22] or fine-tune the strength and directionality of the particle interactions [20, 21, 23]. Space-varying periodic fields are employed to impose constraints on the particle position, forming virtual molds that induce spatial periodic patterns [24–26].

Under external constraints, colloidal suspensions are usually driven out of equilibrium and the relaxation towards equilibrium results from the competition of various mechanisms occurring at different length and time scales. Thus, besides the identification of the equilibrium structures and their dependence on the experimental conditions, it is of paramount practical interest to characterize the kinetic pathways towards the desired structures and the timescales involved.

Part of this thesis is centered in the study of the prototypical example of field-driven self-assembly of colloidal particles. For simplicity, we consider the formation of colloidal bands driven by a periodic (sinusoidal) electromagnetic field and study how the equilibrium structures and the dynamics towards equilibrium depend on the field strength and periodicity, as well as on the particle interactions. We perform extensive Brownian dynamics simulations and complement the study with a coarse-grained analysis based on the dynamic density-functional theory of fluids (DDFT).

Several nontrivial patterns emerge in many particle systems far from equilibrium, where there is an inherent flux. New techniques to characterize these systems have to be developed, making it significantly more challenging than the equilibrium case. Colloids serve has excellent model systems to detect nonequilibrium phase transitions [20].

Here, we are interested in the dynamics driven by a time-varying rotating external field. Rotating magnetic fields can be use to self-organize colloidal particles with permanent dipole moments [27–30]. We study the resilience of lane structures under the rotation of the field. Formation of lanes occur in binary systems of particles that move in opposite directions. They have been observed experimentally in complex plasmas [31, 32], pedestrian traffic [33, 34] and colloidal mixtures [35]. In such systems, lane formation spontaneously occurs to reduce head-on collisions.

We employ Brownian dynamics to simulate colloidal suspensions with particles with symmetrical net charges, where the counter-flow is initially introduced by an uniform external field. Lanes arise from the interplay between the intensity of the field and particle/particle interaction. They are only formed above a critical field intensity [36]. The particle density also plays an important role in lane formation [37]. For low densities the system lacks enough particle collisions to cause a transition, while for high densities the system gets trapped in a jammed configuration. Lanes are only produced for intermediate values. After the initial configuration is formed we switch on the rotational field and study the lane stability.

The thesis is organized as follows: in Chapter 2 we introduce the concepts behind Brownian dynamics and present the model. In Chapter 3 we explain some numerical tricks used to implement the method, while in Chapter 4 we show some tests for the validation of the code. In Chapter 5 we derive the diffusion equation for the band system using two alternative methods: dynamical density functional theory and Fokker-Planck formalism and compare both results. In Chapters 6 and 7 we discuss our findings on self-assembly with a space periodic field and a time-varying field, respectively. Finally, we draw some conclusions in Chapter 8.

Chapter 2

Brownian Dynamics

With the ever growing power and speed of modern computers, as well as efficiency of available algorithms, it is possible to tackle problems with increasing complexity by using numerical methods that are time consuming (or even impossible) to solve by humans. For example, novel phase transitions can be identified and it is possible to draw the phase diagram of new materials [38–40]. But even powerful computers have their own limitations. They have a finite numerical precision, which causes cumulative numerical errors, but more importantly the speed of calculation is limited. While developing a code the computational time that takes to run it is something that we have to consider.

In this thesis we employ Brownian Dynamics to simulate systems of colloidal dispersions. This method consists in the integration of the equations of motion of individual particles subjected to several types of interactions, and it is a suitable numerical technique to study the dynamics of the system. The particles are characterized by their size, shape, charge, polarization, their interactions, etc. They can represent single atoms or complex molecules and a simulation can have multiple species with distinctive properties. By tweaking parameters like temperature or the strength of interaction between particles we can observe how the behavior of the system changes under different conditions.

The information one can get from the simulations is extremely detailed, for example, the trajectories and velocities can be determined for every individual particle. However, our ultimate goal is to produce quantities that can be used to compare to experiments. In most cases the information that is extracted from an experiment with many microscopic particles is a set of averaged macroscopic quantities that can also be calculated in simulations.

We have to be careful when choosing things like the system size, the number of particles, the integration time-step and the type of interactions so that the simulation runs in an adequate time period. There are a number of useful approximations and clever numerical tricks that help reducing considerably the computational time. Some of these however, come with the cost of precision and accuracy so it is important to be confident of how reasonable it is to use them.

Our system is two dimensional (a square with linear size L) and composed of N colloidal particles that interact with each other, with the fluid in which they are suspended and with an external field. We use the Yukawa potential to describe the repulsive interactions between particles and the Langevin formalism to describe their interaction with the fluid. We consider the overdamped regime in which accelerations are neglected.

2.1 Interaction potential

Since colloidal particles have typical sizes of hundreds of nanometers we assume that the classical description is adequate and quantum effects are negligible. There are however colloids with much smaller particles for which this approximation should not be valid. Such systems are beyond the scope of this thesis.

The potential energy of a system V can be represented as a sum of terms that depend on the coordinates of individual particles, pairs, triplets, ...

$$V = \sum_{i} V_1(\vec{r_i}) + \sum_{i}\sum_{j>i} V_2(\vec{r_i},\vec{r_j}) + \sum_{i}\sum_{j>i}\sum_{k>j>i} V_3(\vec{r_i},\vec{r_j},\vec{r}_k) + ... \tag{2.1}$$

where $\vec{r_i}$ is the position of particle i, $\sum_{j>i}$ in the second term on the right-hand side implies that the sum runs over distinct pairs and the summations have a similar meaning on the proceeding terms. The last term of the sum is the one that involves the contribution of the N particles.

V_1 only depends on the position of individual particles (one body term) and it is typically the contribution of an external potential to the overall potential energy, $V_1(\vec{r_i}) = V_{ext}(\vec{r_i})$. In a numerical simulation a term of this type can also be used to impose geometrical confinements (such as a wall that a particle cannot cross). The second term is the potential energy of pairwise interactions. The third term involves triplets and, generally, is smaller than the second term but still has a significant importance in many cases such as in liquids [41]. Higher order terms are expected to be much smaller when compared to V_2 and V_3 and can be confidently neglected. By not considering higher order terms we are neglecting hydrodynamic effects.

The pairwise interaction potential, which (in the simplest case) only depends on the distance between pairs $r = |\vec{r_i} - \vec{r_j}|$, is defined as $V_{ij}(r)$. This potential is used to calculate the forces between particles, and this operation is the one that usually takes longer to perform. The effective pair potential usually describes the interaction in an empirical way and it can depend on the local density, temperature, etc.

Charged colloidal particles are embedded in a fluid that is composed by much smaller particles (from 10 to 10^4 orders of magnitude smaller [42]) that have their own charge and can be polarized, in which case a dipole moment would be induced. The effect is that the original Coulomb potential that would govern the interaction between colloidal particles in the vacuum is screened by the accumulation of counter ions of the fluid in their vicinity. Their interaction potential no longer decays as $\frac{1}{r}$, as it would be expected from the Coulomb potential, but it decays much faster due to the counter ions surrounding the particles. The electromagnetic interactions between particles and particles/fluid is usually described by the Yukawa potential [43, 44]

$$V_{ij}(r) = V_0 \frac{\exp\left(-\alpha r\right)}{r}, \tag{2.2}$$

where V_0 sets the energy scale and the screening parameter α sets the range of the potential. Note that the exponential in this expression makes the Yukawa potential decay much faster than the Coulomb potential.

2.2 Langevin equations

In principle, we can also model the fluid molecules in the same way we model the colloidal particles, accounting for all the Coulomb and dipole interactions. However, from a numerical perspective, this would increase tremendously the computational effort for three reasons. First, the interaction treatment would be more complex. Instead of using a simple Yukawa potential we would need to account for the rotation of all dipoles. Also, the effect of pairwise interactions (solvent/solvent and colloid/solvent) could be long ranged, and we would not be able to take advantage of the short range nature of the interactions to greatly decrease the computational time, as it will be explained in the next chapter. Second, the number of molecules in the fluid is orders of magnitude greater than the number of colloidal particles. With the increase the number of particles, we have to consider more pair interactions, and the simulation takes longer time. Third, the characteristic time-scale of the molecules of the fluid is orders of magnitude shorter than the characteristic dynamical time-scale of the motion of colloidal particles. This means that we would have to adapt the integration of the equations of motion to account for the rapid movement of the fluid molecules by greatly reducing the integration time-step. Within a reasonable simulation time, we would have a good description of the movement of the molecules but the colloidal particles would hardly move at all because their dynamics is much slower. Since we are interested in the behavior of the colloidal particles we need a more appropriate approach.

Instead of considering all the molecules we will treat the fluid as a continuum, in which case the equations of motion of the colloidal particles is described by the Langevin equation [45]

$$m\frac{d\vec{v}}{dt} = -\gamma\vec{v} + \vec{\xi}(t), \tag{2.3}$$

where m is the mass of the particle, $\vec{v}$ is its velocity, γ is the friction coefficient of the medium and $\vec{\xi}$ is a stochastic force. In this and the following sections we will only consider the motion in one dimension (unless stated otherwise) to simplify the notation, but it is straightforward to generalize these results for two and three dimensions, as we did in the simulation. The first term on the right-hand side of Eq. (2.3) is the well known Stokes law that states that the drag force in a viscous fluid is proportional to the velocity [46] and the proportionality parameter is the Stokes friction coefficient γ, which for spherical particles is

$$\gamma = 3\pi\eta d, \tag{2.4}$$

where η is the viscosity of the fluid and d the diameter of the particles. The last term in Eq. (2.3) is the Langevin force that mimics the particle/fluid interaction. This force arises from the collisions between the colloidal particle and the molecules of the fluid that are surrounding it. The collective effect of all collisions is described by a random force sampled from a Gaussian distribution of zero mean, $\langle\xi(t)\rangle = 0$, and second moment that is uncorrelated in time [47]

$$\left\langle\xi(t)\xi(t')\right\rangle = q\delta(t-t') \tag{2.5}$$

where δ is the Dirac delta function which is zero everywhere except for $t = t'$ and with unitary integral from $t = -\infty$ to $t = \infty$. The parameter q establishes the relation between the average kinetic energy of the molecules of the fluid and the motion of the colloids, and therefore should depend on the temperature of the fluid. A trajectory that obeys Eq. (2.3) is called a Brownian trajectory.

We can integrate Eq. (2.3) by imposing an initial condition $v(t = 0) = v_0$, which gives an expression for the velocity [47]

$$v(t) = v_0 e^{-\frac{\gamma}{m}t} + \int_0^t e^{-\frac{\gamma}{m}(t-t')}\frac{\xi(t')}{m}dt'. \tag{2.6}$$

The first term is the solution of the homogeneous equation $\frac{dv}{dt} + \frac{\gamma}{m}v = 0$, and the second term is the particular solution with integrating factor $e^{\frac{\gamma}{m}t}$.

The second moment of the velocities can then be written as

$$\langle v(t_1)v(t_2)\rangle = v_0^2 e^{-\frac{\gamma}{m}(t_1+t_2)} + \frac{q}{m^2}\int_0^{t_1}\int_0^{t_2} e^{-\frac{\gamma}{m}(t_1+t_2-t_1'-t_2')}\delta(t_1'-t_2')dt_1'dt_2'. \qquad (2.7)$$

We can now use the δ integration properties to solve the double integral. The limits of integration of the variable t_1' are 0 and t_1, and analogous for t_2'. We first integrate over the δ. Consequently, the upper limit of the second integration is the smallest time between t_1 and t_2

$$\int_0^{t_1}\int_0^{t_2} ...\, dt_1'dt_2' = e^{-\frac{\gamma}{m}(t_1+t_2)}\int_0^{min(t_1,t_2)} e^{\frac{\gamma}{m}2t'}dt', \qquad (2.8)$$

and the second moment becomes

$$\langle v(t_1)v(t_2)\rangle = v_0^2 e^{-\frac{\gamma}{m}(t_1+t_2)} + \frac{q}{2\gamma m}\left(e^{-\frac{\gamma}{m}|t_1-t_2|} - e^{-\frac{\gamma}{m}(t_1+t_2)}\right). \qquad (2.9)$$

For large t_1 and t_2 we have that $e^{-\frac{\gamma}{m}(t_1+t_2)} \to 0$, and the result becomes independent of the initial condition v_0

$$\langle v(t_1)v(t_2)\rangle = \frac{q}{2\gamma m}e^{-\frac{\gamma}{m}|t_1-t_2|}. \qquad (2.10)$$

This expression allows us to calculate the average energy of a particle

$$\langle E\rangle = \frac{1}{2}m\left\langle v^2\right\rangle = \frac{q}{4\gamma}, \qquad (2.11)$$

and the equipartition law establishes that in the stationary state we have

$$\langle E\rangle = \frac{1}{2}k_BT, \qquad (2.12)$$

where k_B is the Boltzmann constant and T the thermostat temperature of the fluid. Solving for q we arrive to the expression

$$q = 2\gamma k_BT. \qquad (2.13)$$

Therefore, the second moment of the Langevin force is proportional to the temperature

$$\left\langle \xi(t)\xi(t')\right\rangle = 2\gamma k_BT\delta(t-t'). \qquad (2.14)$$

2.3 Mean-square displacement

A useful quantity that is easily measured in a simulation its the mean-square displacement of the Brownian particles. This is also the standard way of measuring the fluctuations of the system. The displacement of a particle can be written as

$$x(t) - x(0) = \int_0^t v(t')dt', \tag{2.15}$$

and the mean-square displacement is

$$\left\langle (x(t) - x(0))^2 \right\rangle = \int_0^t \int_0^t \langle v(t_1)v(t_2) \rangle \, dt_1 dt_2 \tag{2.16}$$

where the second moment of the velocity is given by Eq. (2.9).

Since

$$\int_0^t \int_0^t e^{-\frac{\gamma}{m}(t_1+t_2)} dt_1 dt_2 = \left(\frac{m}{\gamma} \left[1 - e^{-\frac{\gamma}{m}t} \right] \right)^2 \tag{2.17}$$

and

$$\begin{aligned} \int_0^t \int_0^t e^{-\frac{\gamma}{m}|t_1-t_2|} dt_1 dt_2 &= 2 \int_0^t dt_1 \int_0^{t_1} e^{-\frac{\gamma}{m}(t_1-t_2)} dt_2 \\ &= \frac{2m}{\gamma} \left(t - \frac{m}{\gamma} \left[1 - e^{-\frac{\gamma}{m}t} \right] \right), \end{aligned} \tag{2.18}$$

we can write the mean-square displacement as

$$\left\langle (x(t) - x(0))^2 \right\rangle = \left(\frac{m}{\gamma} \left[1 - e^{-\frac{\gamma}{m}t} \right] \right)^2 \left(v_0^2 - \frac{k_B T}{m} \right) + \frac{2k_B T}{\gamma} \left(t - \frac{m}{\gamma} \left[1 - e^{-\frac{\gamma}{m}t} \right] \right). \tag{2.19}$$

Let us now consider that we do not start with a sharp velocity v_0^2 but instead we start already in stationary state with

$$\left\langle v_0^2 \right\rangle = \frac{k_B T}{m}. \tag{2.20}$$

Substituting this result in the mean-square displacement expression the first term becomes zero. For large times we have

$$\left\langle (x(t) - x(0))^2 \right\rangle = \frac{2k_B T}{\gamma} t. \tag{2.21}$$

The mean-square displacement grows linearly in time and with the temperature. Introducing the diffusion coefficient D given by the Einstein relation [48]

$$D = \frac{k_B T}{\gamma}, \tag{2.22}$$

the mean-square displacement becomes

$$\left\langle (x(t)-x(0))^2 \right\rangle = 2Dt. \tag{2.23}$$

2.4 The model

We now return to the two dimensional case. In a colloidal system the viscosity η of the fluid is very high and the inertial force (left-hand side in Eq. (2.3)) is very small in comparison to the drag force. We say that this is the overdamped regime in which the inertial term can be neglected, simplifying the expression, that becomes a first order differential equation of the position $\vec{r}$. An additional interaction force term is added that arises from the potential V acting on a given particle and includes the fluid/particle and the particle/particles interactions

$$\vec{F}_{int} = -\vec{\nabla} V. \tag{2.24}$$

The final equation of motion of particle i in two dimensions is

$$\gamma \frac{d\vec{r}_i}{dt} = -\vec{\nabla}_i \left[\sum_j V_{ij}(r) + V_{ext}(t,\vec{r}_i) \right] + \vec{\xi}_i, \qquad j \neq i \tag{2.25}$$

where the second moment of the Langevin force is $\left\langle \xi_i^k(t)\xi_i^l(t') \right\rangle = 2k_B T\gamma\delta_{kl}\delta(t-t')$. The indices k and l run over the spatial dimensions. Thus, the random force is uncorrelated in time and space. Note that in the last equation we account for the fact that the external potential may also depend on time.

Chapter 3

Numerical Implementation

In this chapter we will focus on the simulation details. The goal behind writing an efficient code is to produce accurate and reliable results in an acceptable time frame. The time that the system takes to enter the regime which displays the phenomena of interest varies from case to case. It mainly depends on the size of the simulation box and the number of particles inside it. It also depends on the type of evolution: the system can relax to an equilibrium state with a fixed structure, or it can evolve to a state far from equilibrium where kinetic structures are formed. We need to ensure the system is large enough to display realistic physical properties, but at the same time, we want to avoid very long simulations. Fortunately, there are a number of numerical tricks and algorithms that we can employ to speed-up our simulations [41, 49, 50].

3.1 Initial conditions

The simulation box is a square domain of linear size L. The way we initially distribute the particles in the domain should be adapted to the type of problem at hand. We are interested in the response of a diffusive system to an external field. The expected initial configuration (in the absence of an external field) is a uniform random distribution of particles over the simulation box.

Because the equation of motion is stochastic, the trajectories of the particles are random and the evolution of one particular simulation will be different from another, even if all the parameters are the same. If we analyze the data from a single evolution the results can display distinctive features that are not characteristic of a typical evolution and only products of statistical fluctuations. To avoid these features the quantities of interest are taken by averaging over many samples.

3.2 Reduced units

It is very helpful to use dimensionless quantities in simulations. This gives us flexibility to choose units in terms of which all physical quantities are expressed. We can, for example, choose a unit of length that is characteristic of the system (e.g. particle radius) and which magnitude is not too different from all the other relevant length scales involved in the problem. This way we can work with numerical values that are close to unity, instead of working with the extremely small values characteristic of nano-scale system in SI units. Numerically, if the values are either too small or too big the precision is seriously affected by rounding and truncation errors.

Another advantage is related to scaling. A model written in reduced units can be used to describe a whole class of problems that include systems with very different length (or energy) scales. Once the properties have been measured in dimensionless units they can be scaled to the appropriate physical units.

We set the unit of length to be the characteristic particle radius, r_p, which can be defined as $r_p = (2\alpha)^{-1}$. The energies and potentials are expressed in units of k_BT and time is defined in units of the Brownian time $\tau = r_p^2\gamma(k_BT)^{-1}$, which is the time over which a colloidal particle diffuses over a region equivalent to its area. The units of density in two dimensions are r_p^{-2} and forces are $k_BTr_p^{-1}$.

3.3 Integration method

To integrate the stochastic differential equations of motion we followed the scheme proposed by Brańka and Heyes [51], which consists of a second-order stochastic Runge-Kutta scheme

$$\vec{r}'_i(t) = \vec{r}_i(t) + \vec{f}_i(\vec{r}_i(t))\frac{\Delta t}{\gamma} + \vec{\xi}_{ri} \tag{3.1}$$

$$\vec{r}_i(t+\Delta t) = \vec{r}_i(t) + \left[\vec{f}_i(\vec{r}_i(t)) + \vec{f}_i(\vec{r}'_i(t))\right]\frac{\Delta t}{2\gamma} + \vec{\xi}_{ri}, \tag{3.2}$$

with a time-step $\Delta t = 10^{-4}\tau$. $\vec{\xi}_{ri}$ is the random displacement vector originated by the Langevin force $\vec{\xi}_i$, which is given by a Gaussian distribution with $\left\langle \vec{\xi}_{ri} \right\rangle = 0$ and $\langle \xi_{ri}^k \xi_{ri}^l \rangle = 2D\Delta t\delta_{kl}$.

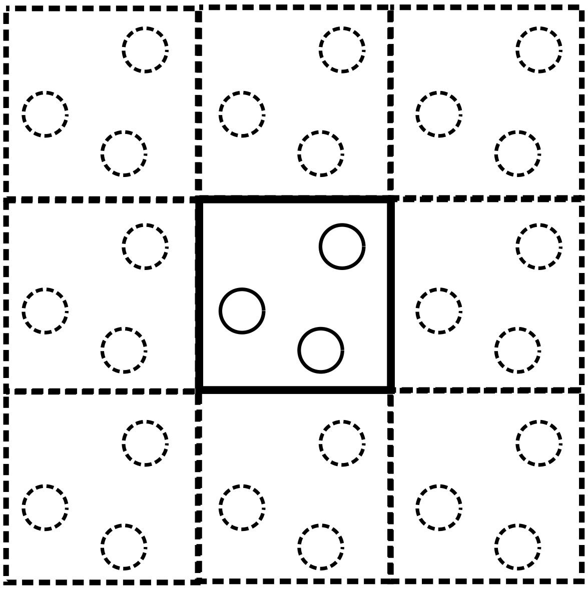

Figure 3.1: Employing periodic boundary conditions is equivalent to considering an infinite system where the domain box is repeated periodically in a square lattice array (adapted from Ref. [41]).

3.4 Periodic boundary conditions and minimum image convention

We are interested in bulk properties which require the use of large systems. To study them properly, we need to guarantee that boundary effects are irrelevant. In the laboratory, the number of particles in a macroscopic sample is sufficiently high and many times it is safe to idealize, for theoretical proposes, that the system is infinite (thermodynamic limit). However, in a simulation the computer resources impose a limit on the number of particles we can use. A better approach is to impose periodic boundary conditions, in which a side of the simulation box is mapped into the opposite side. The introduction of periodic boundaries is equivalent to considering an infinite system where the domain box and its particle configuration is replicated periodically in a square array (Fig. 3.1). With these conditions a particle that crosses the side of the box immediately re-enters in the opposite side. Another consequence, is that while measuring the distance between a pair of particles in the forces computation we need to consider the closest distance (minimum image convention), which might not be the one between the pair in the same domain but the one with the pair which particles are in adjacent copies of the system. Accordingly, a particle near a border interacts more strongly with the particles from the opposite border via the distance that crosses the edge.

But even with periodic boundary conditions, it is still important to be careful with

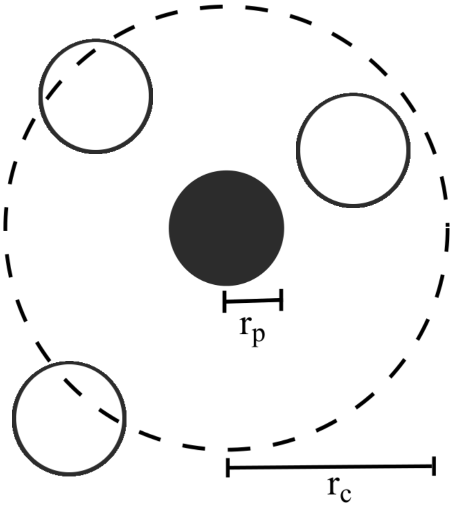

Figure 3.2: Schematic representation of the interaction cut-off distance, r_c. For distances greater than r_c the interactions are neglected.

finite-size effects that can appear when the system is too small. Whenever we chose L, we need to insure that the quantities of interest are not significantly affected by the system size.

3.5 Truncation of the potential

The Yukawa potential decays rapidly (exponentially) with the distance, which means that the forces for pairs above certain distances do not have a big contribution for the overall particles force and there is a lot of time wasted calculating the forces between the N^2 pairs. In fact, the computation of the forces is the most time consuming task in a simulation. We conveniently set a cut-off distance, r_c, above which pairs are neglected (see Fig. 3.2). This truncation greatly reduces the number of expensive computations by neglecting the terms that contribute less for the force of a particle, but it also introduces a discontinuity in the potential at r_c and the force becomes infinite at this point. We can avoid this problem if we shift the potential by its value at the cut-off distance. We can further impose that the force is also continuous by adding a term proportional to the potential derivative at r_c. The final form of the truncated and shifted potential is

$$V_{ij}^{shifted}(r) = \begin{cases} V_{ij}(r) - V_{ij}(r_c) - \left.\frac{dV_{ij}}{dr}\right|_{r=r_c} (r - r_c) & \text{if } r \leq r_c \\ 0 & \text{if } r > r_c \end{cases} \tag{3.3}$$

In Fig. 3.3 we can see how the truncated and shifted potential compares to the simple Yukawa potential.

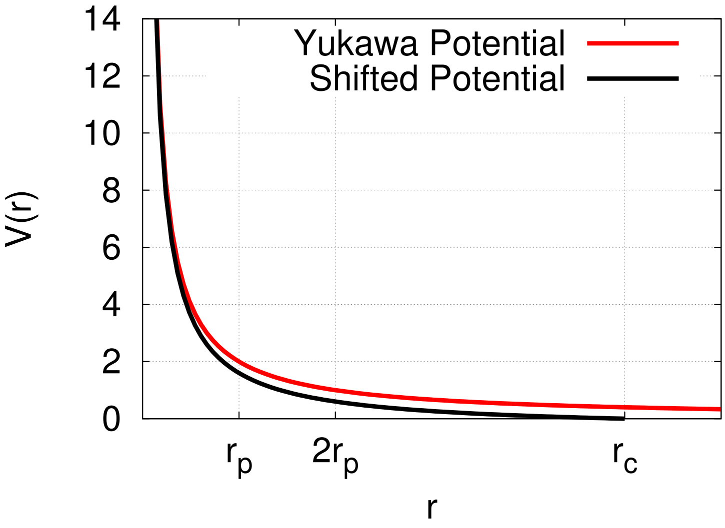

FIGURE 3.3: Comparison between the Yukawa potential and the truncated and shifted version used in the simulations, given by Eq. (3.3).

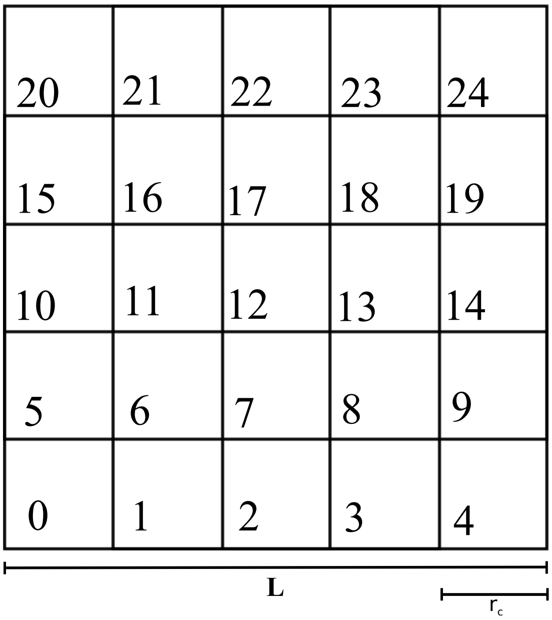

FIGURE 3.4: Cell subdivision of the domain. In this example the cells have exactly size r_c. If we consider a particle that is in cell six we only need to calculate the distance with the particles inside that cell and its immediate neighbors (zero, one, two, five, seven, ten, eleven and twelve) as particles belonging to any other cells are necessarily at distances greater than r_c.

3.6 Cell subdivision and neighbor list

The truncation avoids the calculation of forces over all pairs. This method is still extremely inefficient because we have to calculate the distances between all N^2 pairs and test if they are under the cut-off distance. If r_c is small compared to the system linear size L, only a small percentage of the total number of pairs actually contributes to the sum of the force. The subdivision of the simulation box into small cells is commonly used to identify neighboring particles.

We divide the system into an array of cells as shown in Fig. 3.4. We make the list of the particles that are in each cell, and provided that the side of the cells is equal or greater than r_c, we know that a particle can only interact with the particles that belong to the same cell or the adjacent ones. Because the particles are moving in an erratic way this list needs to be updated every time the forces are calculated.

3.7 Parallelization

Modern computers are built with several processors that can preform tasks in parallel. We can exploit this capability to make the computations in different processors at the same time, which, in most of the cases, speeds-up the simulation when compared to running the code in sequence on one processor only.

Intuitively, it may appear that running on several processors will always be faster than running on a single one, but that is not always the case. Some operations that need to modify a variable several times, like summations and averages, have to be done in sequence, so that there are no ambiguous information coming from different processors. Therefore, the parallelization is a process that needs to be done carefully, and is not applicable to every operation. We can parallelize some sections of the code while others need to run in sequence. The code is initially run on one processor that controls the parallelization process. We call this the master thread. When the code reaches a section that is parallelized the master thread creates a specified number of new threads (called the slave threads) that distribute the computations to different processors. Each slave thread is assigned to one single processor. When the parallelized section finishes, all the computed information is sent to the master thread and the slave threads are deleted. Thread creation and elimination involves some computational power, and it is done several times during a simulation. For this reason, it does not always compensate to parallelize small sections of the code that do not require a lot of resources.

Many times it is possible to modify some parts of the code to make them parallizable, usually at the expense of efficiency. In this occasions, the time that is lost in the efficiency must be compensated by the time gained with the partition of computational work between the processors.

Good candidates for parallelization are “for loops”. We can run several cycles at the same time in different processors as long as we are cautious enough not to include operations that will cause incompatibilities between the threads. Our code was improved with the parallelization of the forces computation and the trajectories integration.

Chapter 4

Code Validation

In this chapter we present some tests to validate our code. It is necessary to study the influence of the mechanisms acting on the particles separately. We first switch off the thermal noise to test of the particle/particle interaction. Then we test the diffusion by switching off interactions between particles.

4.1 Interactions between particles

Without the thermal noise the trajectories of the particles are deterministic as the stochastic part of the equations of motion is eliminated. The simplest test is to set a single particle moving under the influence of a uniform external field. The kinetic energy and trajectory of the particle were monitored. The observed trajectory corresponded to the analytic (straight line in the direction of the force) and the kinetic energy remained constant throughout the integration, as expected for the overdamped regime. In particular, the energy was unchanged while crossing the boundaries of the system, a good indication that the periodic boundary conditions and integration method are properly implemented.

To test the particle/particle interactions we considered a simple test, where particles are initially placed in a square-lattice arrangement and one let the system evolve. With purely repulsive interactions and the lattice symmetry, the net force acting on a particle is zero which means the configuration is stable and the system should remain unchanged. We observed that, as predicted, no particle changed its position and the total kinetic and potential energy remained constant. However, this configuration is unstable so, if we perturb slightly the initial configuration, the system is expected to evolve into a hexagonal-like lattice arrangement, which maximizes the distance between particles

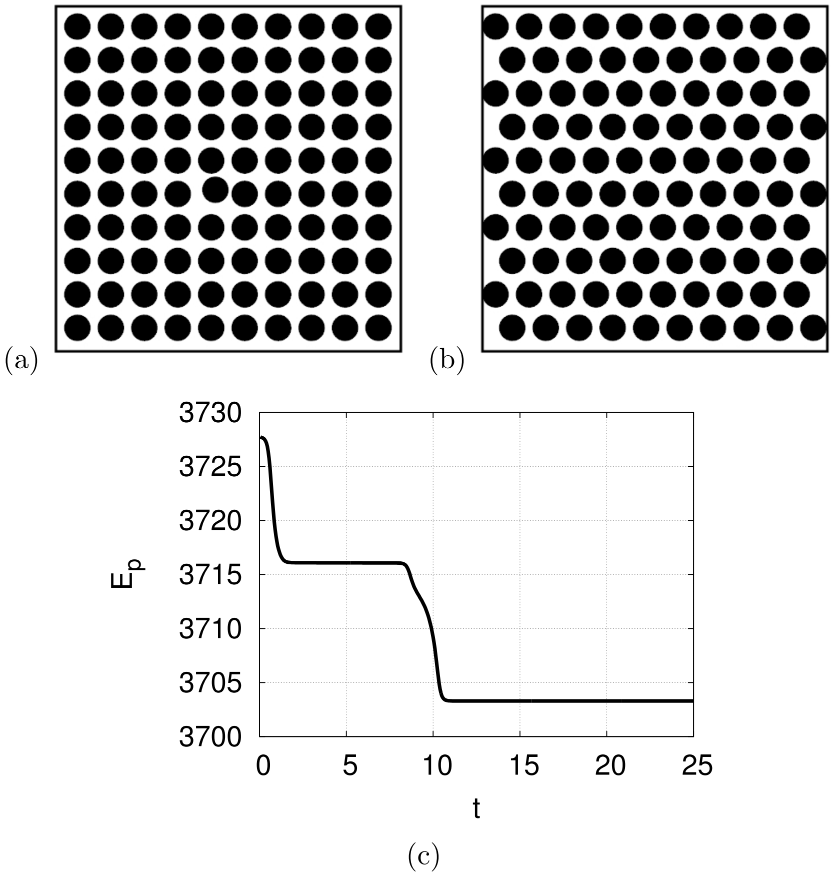

FIGURE 4.1: In (a) the system is at $t = 0$ and the configuration is a square-lattice arrangement with a small defect. As it evolves, the system goes into a more stable, hexagonal-like, configuration showed in (b) at $t = 15$. In (c) is plotted the potential energy throughout the evolution.

in one direction, while keeping the density constant. This process is demonstrated in Fig. 4.1 where the initial state in (a) is a square-lattice arrangement with one particle deviated from the respective position. In (b) is a state in a later time with a hexagonal-like lattice. In (c) the total potential energy decreases to a lower value while going from the state in (a) into the state in (b) (the system also passes through a metastable state as indicated by the intermediate plateau). Since the potential energy is in fact the interaction potential, which decreases with the distance between pairs of particles, the plot shows that the more stable configuration is the one that, on average, has the largest inter-particle separation.

All these tests suggest that the integration, periodic boundary conditions, minimum image convention and the particle/particle interaction were implemented successfully.

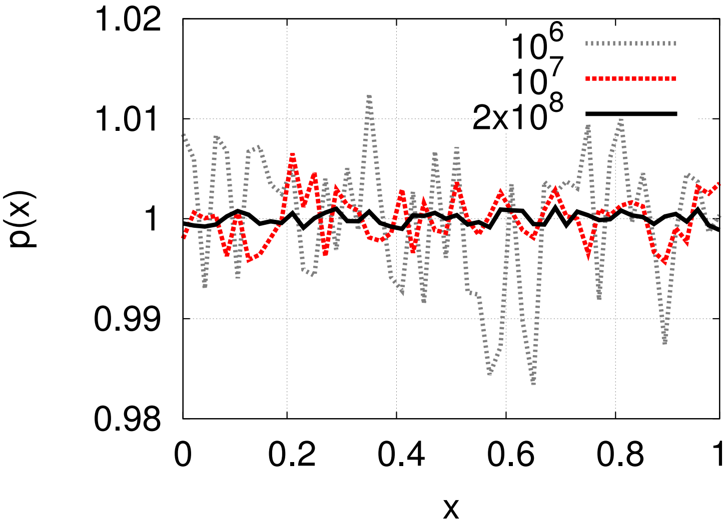

FIGURE 4.2: Normalized histograms of a set of 10^6 numbers (red), 10^7 numbers (green) and 2×10^8 numbers provided by the Mersenne-Twister method.

4.2 Thermal noise

In the physical system, thermal noise arises from the interaction between the particles and the fluid. A particle is constantly being "pushed" around in all directions by the much smaller and numerous molecules that compose the fluid. This effect can be described in simulations by a random force that is applied at every time-step. Along with the addition of the drag term caused by the viscosity of the fluid we have a way to accurately represent the particle/fluid interaction.

A crucial part of a Brownian dynamics simulation is the generation of random numbers. As before, we isolate this effect by switching off the particle/particle interactions, consequently the particles behave as a perfect gas.

Pseudorandom number generators (PRNG) return a sequence of approximately uncorrelated numbers by providing a seed value to a computational algorithm. The sequence has an intrinsic periodicity and the numbers are not truly random because given the same seed the PRNG will return the same sequence of "random" values. Therefore it is important to use a method with a large period and capable of producing (ideally) uncorrelated sequences of numbers. We generate uniformly distributed random numbers using the Mersenne-Twister (MT) algorithm provided by the Boost C++ source libraries [52]. The MT method is implemented with a maximum period of $2^{19937} - 1$ and it has passed various statistical tests [53]. Because of the highly uncorrelated sequence of numbers, large period and its speed, the MT algorithm is the most extensively used PRNG.

We made the histograms of several series of numbers generated by the MT algorithm to confirm their distribution is uniform, the results are plotted in Fig. 4.2. We observe that the distribution of numbers in the interval $[0, 1]$ converges to a uniform distribution with the increase of generated numbers.

We are interested, however, in generating random numbers with a Gaussian distribution that represent the displacements ξ_r

$$p(\xi_r) = \frac{1}{\sigma\sqrt{2\pi}} e^{-\frac{(\xi_r - \langle \xi_r \rangle)^2}{2\sigma^2}}, \tag{4.1}$$

as discussed in the previous section. We make use of the Box-Muller method [54]

$$\xi_r = \langle \xi_r \rangle + \sqrt{-2\sigma^2 \ln R_1} \cos(2\pi R_2) \tag{4.2}$$

that transforms two random numbers that are uniformly distributed, R_1 and R_2, into one random displacement with a Gaussian distribution, with variance σ^2 and mean $\langle \xi_r \rangle$. Brownian motion as an associated variance of $\sigma^2 = 2Dt$. The dots in Fig. 4.3 (a) show the normalized distribution of 2×10^8 displacements with mean $\langle \xi_r \rangle = 0$ and variance $\sigma^2 = 5 \times 10^{-4}$, calculated with the Box-Muller transform. We confirm that the distribution is indeed a Gaussian.

We expect that their velocities follow a Maxwell-Boltzmann distribution in two dimensions. We know that the velocities in each direction v_x and v_y also have a Gaussian distribution

$$p(v_i) = \frac{1}{\sigma_v\sqrt{2\pi}} e^{-\frac{v_i^2}{2\sigma_v^2}}, \tag{4.3}$$

where i stands for the x or y directions and σ_v^2 is the velocity variance which relates with the displacement variance with $\sigma_v^2 = \sigma^2/t^2 = 2D/t$. The probability distributions in both directions are independent and the probability distribution of the total velocity $v = \sqrt{v_x^2 + v_y^2}$ is $p(v) = p(v_x)p(v_y)$ with an area element of $v d\theta dv$. Making the integration in θ we arrive to the expression of the two dimensional Maxwell-Boltzmann distribution

$$p(v) = \frac{v}{\sigma_v^2} e^{-\frac{v^2}{2\sigma_v^2}}. \tag{4.4}$$

Figure 4.3 (b) shows that the velocity of the particles follows the Maxwell-Boltzmann distribution.

Figure 4.4 (a) shows the average total displacement of a particle $\langle r \rangle$ for different temperatures. Since the distribution of displacements at each time-step has zero mean, we expect that $\langle r \rangle$ is also zero, and the result should be independent from the thermostat temperature, which can be confirmed by the figure. We have seen in the previous

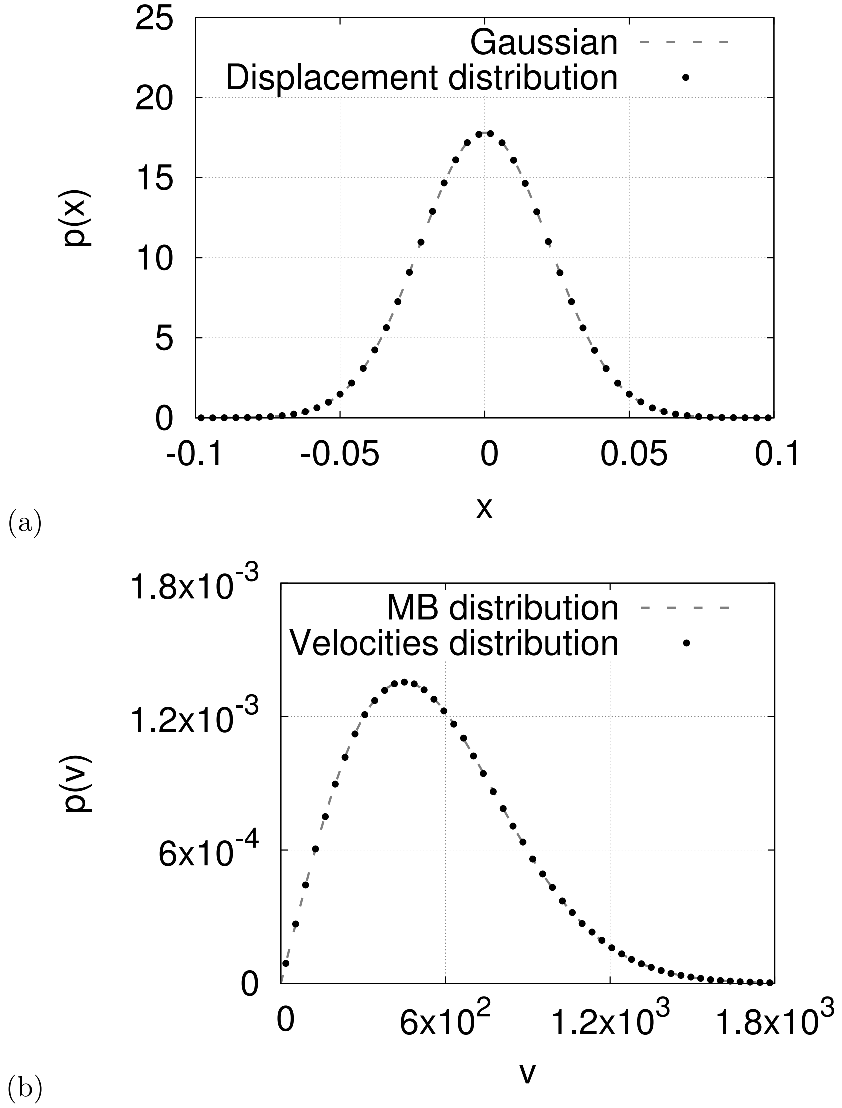

FIGURE 4.3: (a) Displacement distribution with mean $\langle \xi_r \rangle = 0$ and variance $\sigma^2 = 5 \times 10^{-4}$ calculated with the Box-Muller method and the respective Gaussian. (b) Velocity distribution with $\sigma_v^2 = 2 \times 10^5$ and the respective Maxwell-Boltzmann distribution. The results are in perfect agreement with the expected distributions.

chapter that each degree of freedom contributes with $2Dt$ to the second moment of the displacement. The diffusion coefficient for two dimensions is then given by the following expression

$$D = \frac{< r^2 > - < r >^2}{4t} \tag{4.5}$$

and see its dependence on the temperature. The Stokes-Einstein relation $D = k_B T/\gamma$ tells us that the diffusion coefficient is proportional to the temperature in accordance with Fig. 4.4 (b) result.

Finally, we can preform some tests to see if there are correlations between the random

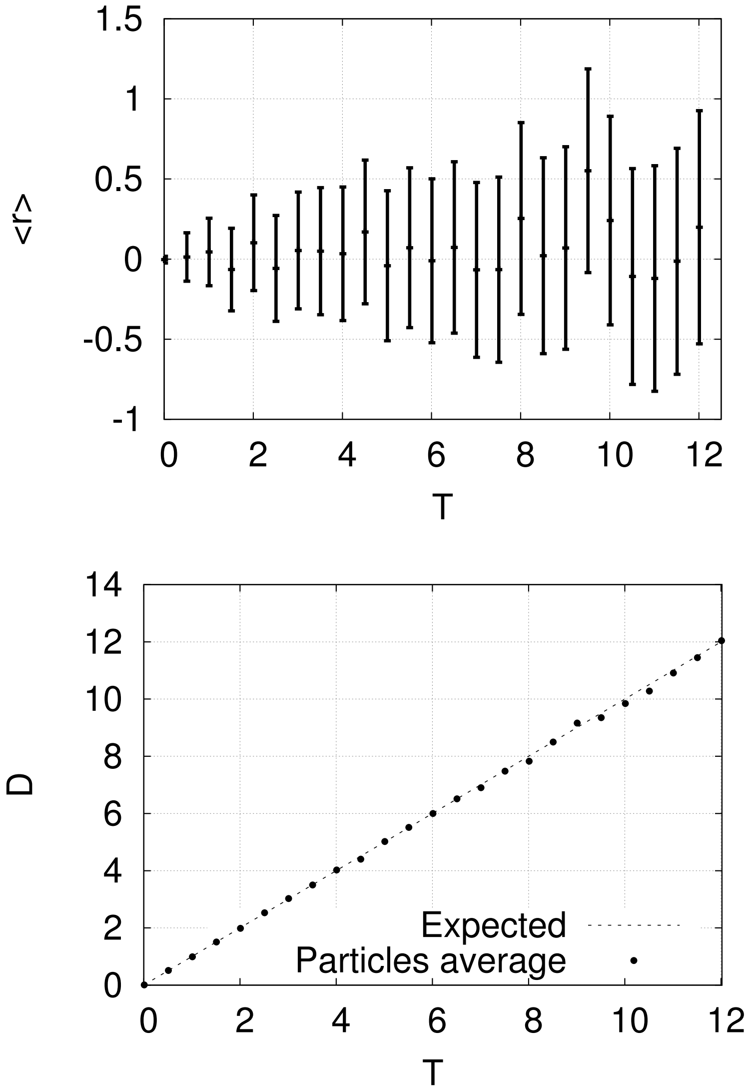

(a)

(b)

FIGURE 4.4: (a) Average total displacement $\langle r \rangle$ of 4000 particles and 50000 time-steps for different temperatures. (b) Diffusion coefficient of the particles for $k_B = 1$ and $\gamma = 1$.

numbers that we are generating. We already discussed that the MT algorithm was extensively tested. However, we want to check if the operation we use to transform random numbers from a uniform distribution to random numbers from a Gaussian distribution does not compromise the lack of correlation between numbers.

We start by plotting in Fig. 4.5 (a) the random numbers in a sequence in function of the preceding value, $x_{i+1}(x_i)$, and we see that the points are distributed in a circle area around zero, with the point density decreasing with the distance to the origin, which is a consequence of the Gaussian distribution of the points and confirms that there is no correlation. This method has the disadvantage of only testing the correlation between adjacent values in the sequence in a graphical fashion. To make a more quantitative test

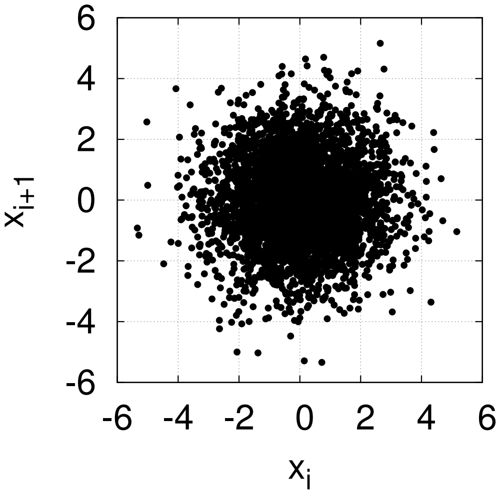

(a)

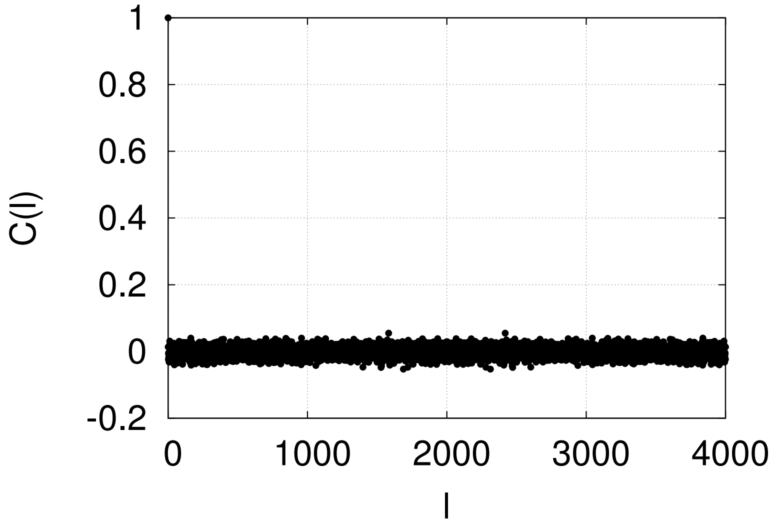

(b)

FIGURE 4.5: (a) Graphical test of the correlations between the values in a sequence x_i of 4000 Gaussian distributed random numbers. (b) Correlation coefficient for the same sequence.

we calculate the correlation coefficient defined as

$$C(l) = \sum_{l=0}^{N-1} \frac{\langle x_i x_{i+l} \rangle - \langle x_i \rangle \langle x_{i+l} \rangle}{\sigma_i \sigma_{i+l}}, \tag{4.6}$$

where the averages $\langle ... \rangle$ are done over the index $i = 0...N-1$ and

$$\sigma_i = \sqrt{\frac{\sum_i^N (x_i - \langle x_i \rangle)^2}{N}}, \qquad \sigma_{i+l} = \sqrt{\frac{\sum_i^N (x_{i+l} - \langle x_{i+l} \rangle)^2}{N}} \tag{4.7}$$

with identical definition for σ_l. The results are found in Fig. 4.5 (b). If x_i and x_l are uncorrelated then $\langle x_i x_{i+l} \rangle = \langle x_i \rangle \langle x_{i+l} \rangle$, because the points are distributed with a

Gaussian with zero mean we have in particular that $\langle x_i \rangle = 0$. We see that the correlation factor is one when $l = 0$ and approximately zero for all the other values, showing that the correlation is weak.

Chapter 5

From Discrete to Continuum Description

5.1 The diffusion equation

The trajectories given by Eq. (2.25) will provide the positions of every particle during the simulation. We can use this microscopic information to derive the macroscopic local density of particles $\rho(t, \vec{r})$, which is the average number of particles in position $\vec{r}$ at time t. The complete coarse-grained description of the system is given when we derive the evolution equation for $\rho(t, \vec{r})$.

Since the number of particles is conserved, we can use the continuity equation

$$\frac{\partial \rho(t, \vec{r})}{\partial t} + \vec{\nabla}.\vec{j}(t, \vec{r}) = 0, \tag{5.1}$$

where $\vec{j}(t, \vec{r})$ is the flux of density. In a system without particle/particle interactions, this flux has a contribution from the thermal diffusion $\vec{j}_{diffusion}$ and another, $\vec{j}_{drift}$, that is caused by the presence of an external field $V_{ext}(r)$.

The drift flux has the usual form

$$\vec{j}_{drift} = \vec{v}\rho(\vec{r}) \tag{5.2}$$

where, in the overdamped regime, the velocity $\vec{v}$ is imposed by the external potential that originates a force $\vec{F}_{ext} = -\vec{\nabla} V_{ext}$. The total force acting on a particle is zero and the forces that arise from an external potential obey the relation $\vec{F}_{ext} = \gamma\vec{v}$.

The Fick's law [46] states that the flux due to the diffusion is proportional to the gradient of the density, and the proportionality is given by the diffusion coefficient

$$\vec{j}_{diffusion} = -D\vec{\nabla}\rho(\vec{r}). \tag{5.3}$$

This result implies that particles move to regions of lower density in the absence of any external field.

The density evolution equation, which is also known as the diffusion equation, becomes

$$\frac{\partial \rho(t,\vec{r})}{\partial t} = D\nabla^2\rho(t,\vec{r}) - \vec{\nabla}.(\vec{v}\rho(t,\vec{r})), \tag{5.4}$$

where, for simplicity, we assume that the diffusion coefficient D is independent of the position.

Note that in the stationary state $\frac{\partial \rho}{\partial t} = 0$

$$\rho(\vec{r}) = \rho_0 e^{-\frac{V_{ext}(\vec{r})}{k_B T}} \tag{5.5}$$

is a solution of the diffusion equation, and we obtain the Boltzmann statistics that we expect to find when the system is at equilibrium. The constant ρ_0 corresponds to the density of the system where $V_{ext}(\vec{r}) = 0$ or when the temperature is infinite.

We will derive the complete diffusion equation where we also include the particle/particle interactions, but first lets consider the system in equilibrium.

5.2 Density-functional theory

An approximation for the Helmholtz free energy functional can be written as

$$\begin{aligned} \mathcal{F}[\rho] = & \int k_B T\rho(\vec{r}) \left[\log\left(\rho(\vec{r})\Lambda^2\right) - 1\right] d\vec{r} \\ & + \frac{1}{2}\int\int \rho(\vec{r})\rho(\vec{r}\,')V_{ij}(\vec{r}-\vec{r}\,')d\vec{r}\,'d\vec{r} \\ & + \int \rho(\vec{r})V_{ext}(\vec{r})d\vec{r}. \end{aligned} \tag{5.6}$$

On the right-hand side, the first term is the free energy of the ideal gas where Λ is the thermal de Broglie wavelength, the second term is the mean-field approximation to the contribution from the interactions and the last term is the external potential contribution.

We use the local density approximation (LDA) by setting $\rho(\vec{r}\,') \simeq \rho(\vec{r})$ which is a good assumption if the density is a smooth function of the position.

The chemical potential is the functional derivative of the free energy

$$\begin{aligned}\mu &= \frac{\delta \mathcal{F}}{\delta \rho(\vec{r})} \\ &= \frac{\partial L}{\partial \rho(\vec{r})} - \frac{d}{d\vec{r}}\left(\frac{\partial L}{\partial \nabla \rho(\vec{r})}\right),\end{aligned} \tag{5.7}$$

where L in the second equality is defined as

$$\mathcal{F} = \int L[\vec{r}, \rho(\vec{r}), \nabla\rho(\vec{r})] d\vec{r}. \tag{5.8}$$

Note that the LDA approximation is equivalent to consider the density expansion $\rho(\vec{r}\,') \simeq \rho(\vec{r}) + \nabla\rho(\vec{r})(\vec{r} - \vec{r}\,')$, since after the derivation the first order term vanishes. The chemical potential is

$$\mu = k_B T \log\left(\rho(\vec{r})\Lambda^2\right) + A\rho(\vec{r}) + V_{ext}(\vec{r}), \tag{5.9}$$

where A is the interaction parameter that quantifies the pairwise interactions, which we define as

$$A = \int V_{ij}(\vec{r}) d\vec{r} \tag{5.10}$$

expressed in units of $k_B T r_p^2$. Rearranging Eq. 5.9 we find an expression for the density profile

$$\rho(\vec{r}) = Z \exp[-\beta\left(V_{ext} + A\rho(\vec{r})\right)] \tag{5.11}$$

where $\beta = (k_B T)^{-1}$ and $Z = \Lambda^{-2} e^{\beta\mu}$ is a normalization constant that represents the density of an ideal gas with chemical potential μ. We used the Picard method to solve this equation, with an additional constraint $N = \int \rho(\vec{r}) d\vec{r}$ arising from the conservation of the total number of particles.

5.3 Dynamic density-functional theory

If we consider that the system evolves adiabatically, the evolution equation of the local density can be written directly from the equilibrium Helmholtz free energy functional [55, 56],

$$\gamma \frac{\partial \rho(\vec{r}, t)}{\partial t} = \vec{\nabla} . \left[\rho(\vec{r}, t) \vec{\nabla} \frac{\delta \mathcal{F}[\rho(\vec{r}, t)]}{\delta \rho(\vec{r}, t)}\right]. \tag{5.12}$$

Using the functional defined in Eq. (5.6), we obtain a diffusion equation for the density,

$$\gamma \frac{\partial \rho}{\partial t} = \vec{\nabla} . \left[A\rho \vec{\nabla}\rho + \vec{\nabla} V_{ext} \rho\right] + k_B T \nabla^2 \rho \ \ , \tag{5.13}$$

where the first and last terms are related to the particle/particle and particle/fluid interactions, respectively. They tend to smooth out any spatial variation of the density. The middle term is related to the particle/field interaction. Note that, when one applies $\vec{\nabla}.$ to the first term one gets $A\rho\nabla^2\rho$, a non-linear diffusion term where the coefficient increases with the density. It is the interplay of the thermostat temperature, external potential and particle/particle interactions that controls the kinetics of relaxation and defines the relaxation time towards the stationary state.

5.4 Fokker-Planck derivation

The diffusion equation can also be obtained in an alternative way using the Fokker-Planck formalism [57]. We start by defining the function $P(\vec{r}_1, ..., \vec{r}_N, t)$ as the probability density of finding the particles 1, 2, ... , N in positions $\vec{r}_1$, $\vec{r}_2$, ... , $\vec{r}_N$ at time t. The Fokker-Planck equation that describes the evolution of $P(\vec{r}_1, ..., \vec{r}_N, t)$ is

$$\frac{\partial P}{\partial t} = \sum_i^N \vec{\nabla}_i.(-\vec{v}_i P + D\vec{\nabla}_i P), \tag{5.14}$$

where $\vec{v}_i$ is the velocity of particle i.

Function $P(\vec{r}_1, ..., \vec{r}_N, t)$ describes the state of the system in the configuration space with $2N$ dimensions. Our goal is to outline the evolution of the density of particles $\rho(\vec{r}, t)$ in the space with two spatial dimensions. This density is defined as the average over all possible system configurations weighted by the probability density function $P(\vec{r}_1, ..., \vec{r}_N, t)$

$$\begin{aligned}\rho(\vec{r}, t) &\equiv \left\langle \sum_i^N \delta(\vec{r} - \vec{r}_i) \right\rangle \\ &= \int d^N\vec{r}\,' P(\vec{r}\,'_1, ..., \vec{r}\,'_N, t) \sum_i^N \delta(\vec{r} - \vec{r}\,'_i),\end{aligned} \tag{5.15}$$

where $\delta(\vec{r} - \vec{r}_i)$ is the δ-Dirac function. The evolution of the particle density can be written in the following way

$$\frac{\partial \rho(\vec{r}, t)}{\partial t} = \int d^N\vec{r}\,' \frac{\partial P}{\partial t} \sum_i^N \delta(\vec{r} - \vec{r}\,'_i). \tag{5.16}$$

Now we can use Eq. (5.14) in Eq. (5.16) to obtain,

$$\frac{\partial \rho(\vec{r}, t)}{\partial t} = \int d^N\vec{r}\,' \sum_m^N \vec{\nabla}'_m.(-\vec{v}\,'_m P + D\vec{\nabla}'_m P) \sum_i^N \delta(\vec{r} - \vec{r}\,'_i). \tag{5.17}$$

The integration of the δ-Dirac function ensures that the only terms that are different from zero are the ones with spatial derivatives with $m = i$ and we rewrite Eq. (5.17)

$$\frac{\partial \rho(\vec{r},t)}{\partial t} = \int d^N\vec{r}\,' \sum_{i}^{N} \vec{\nabla}'_i.(-\vec{v}\,'_i P + D\vec{\nabla}'_i P)\delta(\vec{r} - \vec{r}\,'_i). \tag{5.18}$$

From the properties of the δ-Dirac function, for two general functions $f(x)$ and $g(x)$, we have that

$$\begin{aligned} g(x)\int dx' f(x')\delta(x-x') &= \int dx' g(x')\delta(x-x') \int dx' f(x')\delta(x-x') \\ &= \int dx' g(x') f(x')\delta(x-x'). \end{aligned} \tag{5.19}$$

Using this relation we can bring the spatial derivative outside of the integral

$$\frac{\partial \rho(\vec{r},t)}{\partial t} = -\vec{\nabla}.\sum_{i}^{N}\int d^N\vec{r}\,'\vec{v}\,'_i P\delta(\vec{r}-\vec{r}\,'_i) + D\nabla^2\int d^N\vec{r}\,' P \sum_{i}^{N}\delta(\vec{r}-\vec{r}\,'_i), \tag{5.20}$$

that can be written as a diffusion equation

$$\frac{\partial \rho(\vec{r},t)}{\partial t} = -\vec{\nabla}.\vec{j} + D\nabla^2\rho(\vec{r},t) \tag{5.21}$$

with flux

$$\vec{j} = \sum_{i}^{N}\int d^N\vec{r}\,'\vec{v}\,'_i P\delta(\vec{r}-\vec{r}\,'_i). \tag{5.22}$$

Since the diffusion is already included in the second term of Eq. (5.21), this time $\vec{j}$ has a contribution that comes from the interaction with an external potential and another from the interaction between particles, $\vec{j} = \vec{j}_{ext} + \vec{j}_{int}$.

The external density flux can then be written

$$\vec{j}_{ext} = \frac{1}{\gamma}\int d^N\vec{r}\,' \sum_{i}^{N}\vec{F}_{ext}(\vec{r}\,'_i)P\delta(\vec{r}-\vec{r}\,'_i). \tag{5.23}$$

Using once again the relation in Eq. (5.19) we have

$$\begin{aligned} \vec{j}_{ext} &= \frac{1}{\gamma}\vec{F}_{ext}(\vec{r})\int d^N\vec{r}\,'\sum_{i}^{N} P\delta(\vec{r}-\vec{r}\,'_i) \\ &= \frac{1}{\gamma}\vec{F}_{ext}(\vec{r})\rho(\vec{r},t). \end{aligned} \tag{5.24}$$

Note that the density flux is simply proportional to $\rho(\vec{r},t)$ and it will contribute with a linear term to Eq. (5.21).

We now make a similar treatment for the interaction flux. The interaction force does not only depend on the position of a single particle but is a function of the distance between pairs of particles, $\vec{F}_{int} = \vec{F}_{int}(\vec{r}_i - \vec{r}_j)$. The interaction density flux is

$$\begin{aligned} \vec{j}_{int} &= \frac{1}{\gamma}\sum_i^N \int d^N\vec{r}\,' \sum_{i\neq j}^N \vec{F}_{int}(\vec{r}\,'_i - \vec{r}\,'_j) P \delta(\vec{r} - \vec{r}\,'_i) \\ &= \frac{1}{\gamma}\sum_i^N \int d^N\vec{r}\,' \sum_{i\neq j}^N \vec{F}_{int}(\vec{r} - \vec{r}\,'_j) P \delta(\vec{r} - \vec{r}\,'_i). \end{aligned} \tag{5.25}$$

The second equality is a result of operating the δ-function on $\vec{F}_{int}$. It is possible to rewrite the interaction force as

$$\vec{F}_{int}(\vec{r} - \vec{r}\,'_j) = \int d\vec{r}\,''\vec{F}_{int}(\vec{r} - \vec{r}\,'')\delta(\vec{r}\,'' - \vec{r}\,'_j) \tag{5.26}$$

and the interaction density flux becomes

$$\vec{j}_{int} = \frac{1}{\gamma}\int d^N\vec{r}\,''\vec{F}_{int}(\vec{r} - \vec{r}\,'') \int d^N\vec{r}\,' \sum_i^N \sum_{i\neq j}^N \delta(\vec{r}\,'' - \vec{r}\,'_j) P \delta(\vec{r} - \vec{r}\,'_i). \tag{5.27}$$

The last integral is defined to be the two point correlation function

$$\rho^{(2)}(\vec{r},\vec{r}\,'',t) \equiv \int d^N\vec{r}\,' \sum_i^N \sum_{i\neq j}^N \delta(\vec{r}\,'' - \vec{r}\,'_j) P \delta(\vec{r} - \vec{r}\,'_i). \tag{5.28}$$

This expression can be written in terms of the three point correlation function, and in turn, this one can be written in terms of the four point correlation function, and so on. We use the simplest truncation scheme in which we assume that the density is a local function, i.e., the density in point $\vec{r}$ is independent of the density in $\vec{r}\,''$

$$\rho^{(2)}(\vec{r},\vec{r}\,'',t) = \rho(\vec{r},t)\rho(\vec{r}\,'',t) \tag{5.29}$$

and Eq. (5.27) assumes the following form

$$\vec{j}_{int} = \frac{1}{\gamma}\rho(\vec{r},t)\int d\vec{r}\,''\vec{F}_{int}(\vec{r} - \vec{r}\,'')\rho(\vec{r}\,'',t). \tag{5.30}$$

To write the evolution equation of $\rho(\vec{r},t)$ in a useful form, we still need to remove the dependency on $\vec{r}\,''$. We simplify the last expression by further assuming that the density does not change considerably in the area surrounding a particle because, in our system, the intensity of the interaction among particles decays very rapidly with the distance. This allow us make first order expansion of $\rho(\vec{r}'', t)$ at $\vec{r}$

$$\vec{j}_{int} = \frac{1}{\gamma}\rho(\vec{r}, t) \int d\vec{r}'' \vec{F}_{int}(\vec{r} - \vec{r}'') \left[\rho(\vec{r}, t) + \vec{\nabla}\rho(\vec{r}, t).(\vec{r}'' - \vec{r})\right]. \tag{5.31}$$

The first term on the right hand side is zero because it is the integral of a radial function

$$\int dr\, h(r) \int_0^{2\pi} d\varphi(\cos(\varphi)\hat{x} + \sin(\varphi)\hat{y}) = 0 \tag{5.32}$$

where $h(r)$ is the radial part of the integrand and the integral of the sine and cosine functions is zero over a complete period. We now make the substitution $\vec{l} = \vec{r}'' - \vec{r}$ and Eq. (5.31) becomes

$$\vec{j}_{int} = -\frac{1}{\gamma}\rho \int d\vec{l}\, \vec{F}_{int}(\,\vec{l}\,)\, \vec{\nabla}\rho \,.\, \vec{l}, \tag{5.33}$$

note that the sign ensures that $\vec{F}_{int}$ is parallel to $\vec{l}$. We now consider that $\hat{u}$ is the direction parallel to $\vec{\nabla}\rho$ and $\hat{w}$ the perpendicular direction. We can then make the projection of any vector in the direction of $\vec{l}$ into the new reference frame

$$\hat{l} = \cos(\varphi)\, \hat{u} + \sin(\varphi)\, \hat{w} \tag{5.34}$$

where φ is the angle between $\vec{l}$ and $\vec{\nabla}\rho$. The integral in Eq. (5.33) is then

$$\int d\vec{l}\, \vec{F}_{int}(\,\vec{l}\,)\, \vec{\nabla}\rho \,.\, \vec{l} = \int dl |\vec{F}_{int}||\vec{\nabla}\rho| l^2 \int d\varphi(\cos(\varphi)\cos(\varphi)\, \hat{u} + \sin(\varphi)\cos(\varphi)\, \hat{w}), \tag{5.35}$$

where $l = |\vec{l}|$. The second term of the angular part on the right hand side becomes zero when we integrate it over all directions, therefore contributions perpendicular to $\vec{\nabla}\rho$ vanish. The integration of the other angular term yields π. The result is then a vector proportional to $\vec{\nabla}\rho$

$$\begin{aligned} \vec{j}_{int} &= -\frac{1}{\gamma}\rho\vec{\nabla}\rho\pi \int dl |\vec{F}_{int}| l^2 \\ &= -\frac{1}{\gamma}\rho\vec{\nabla}\rho\frac{1}{2} \int d\vec{l}\, \vec{F}_{int} \,.\, \vec{l}, \end{aligned} \tag{5.36}$$

and we define the constant a as

$$a = \frac{1}{2} \int d\vec{l}\, \vec{F}_{int} \,.\, \vec{l}, \tag{5.37}$$

which measures the strength of the interaction between particles. Considering the diffusion coefficient $D = \frac{k_B T}{\gamma}$, the final evolution equation for the density of particles is

$$\gamma \frac{\partial \rho(\vec{r}, t)}{\partial t} = \vec{\nabla}.(a\rho\vec{\nabla}\rho - \vec{F}_{ext}\rho) + k_B T \nabla^2 \rho(\vec{r}, t). \tag{5.38}$$

5.5 Comparison between DDFT and Fokker-Planck derivations

The diffusion equation derived from the DDFT, Eq. (5.13), is equivalent to the one derived from the Fokker-Planck formalism, Eq. (5.38). The only thing that distinguishes them is the parameters of interaction given by

$$A = \int V_{ij}(\vec{r}) d\vec{r} \tag{5.39}$$

and

$$a = -\frac{1}{2} \int \vec{\nabla} V_{ij} \, . \, \vec{r} \, d\vec{r}, \tag{5.40}$$

respectively. Both of them depend only on the interaction potential. We can calculate explicitly a for the Yukawa potential. The force of interaction is

$$\vec{F}_{int} = V_0 \frac{\exp(-\alpha r)}{r^2} \left(\alpha + \frac{1}{r} \right) \vec{r}. \tag{5.41}$$

We substitute this result on Eq. (5.37) and after the integration over all space we get

$$a = 2\pi \frac{V_0}{\alpha}, \tag{5.42}$$

and the same result can be calculated for A. The interaction parameters only depend on the ratio between the parameter V_0 that controls the strength of the interaction and the parameter α that controls its range. Also, they are independent of the system parameters, such as the system size or temperature. These are integrated quantities that are space independent. We established a mean-field theory that associates the collective effect that all particles have on the local density with a scalar.

However, in the simulations we use the truncated and shifted potential from Eq. (3.3). In figures 5.1 and 5.2 we show the interaction parameters calculated with this potential. The curves of both parameters coincide for all V_0 and α, showing a remarkable consistency between both formalisms. The figures also show that the interaction grow linearly with V_0 and it is inversely proportional to α for high α.

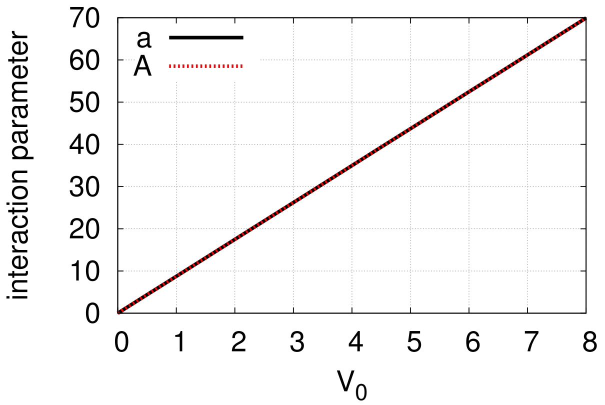

FIGURE 5.1: Interaction parameters a and A for different V_0. The screening parameter is $\alpha = 0.5$ and the cut-off distance is $r_c = 5$.

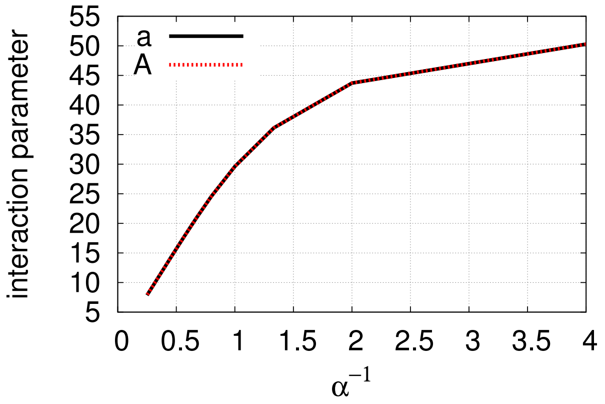

FIGURE 5.2: Interaction parameters a and A for different α. The screening parameter is $V_0 = 5$ and the cut-off distance is $r_c = 5$.

This equality does not hold for potentials of other kinds. Take for example the Coulomb potential $V = V_0/r$. The interaction parameters differ by a factor of two: $A = 2\pi V_0 r_c$ and $a = \pi V_0 r_c$.

5.6 Channel with particles: test

Let us now consider a simple setup that allow the comparison between the coarse-grained model we just derived and numerical simulations. The domain is a closed channel that is wider in the x-direction with a wall at $x = 0$. We apply a constant external force in the x-direction towards the wall. We start with a random space distribution and under the action of the external force the particles will accumulate near the wall at $x = 0$ (top panel in Fig. 5.3). We will consider the system in the stationary state and neglect

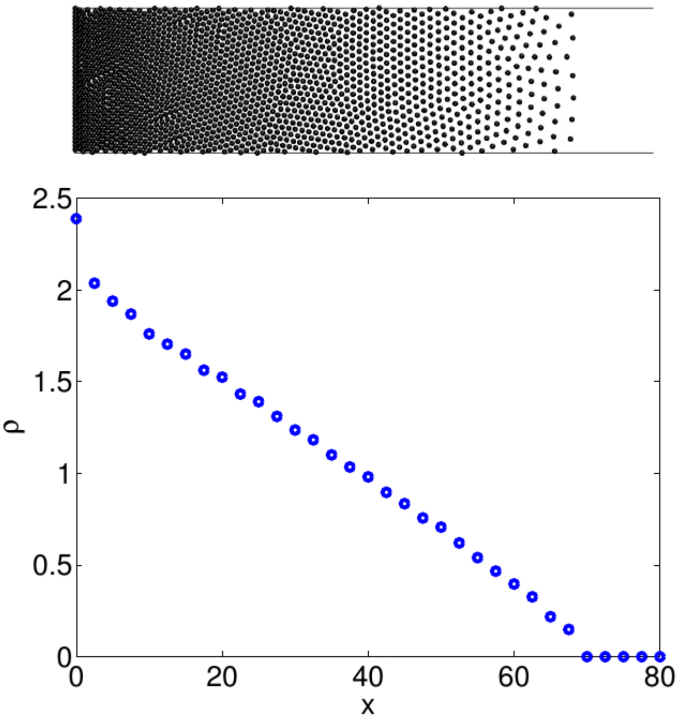

FIGURE 5.3: The top panel shows the equilibrium state of a channel simulation with $V_0 = 5$, $\alpha = 0.5$ and $F_{ext} = -1$. The size of the system in the y-direction is 20. The bottom panel shows the respective density profile in the x-direction.

thermal fluctuations. Eq. (5.38) becomes

$$\vec{j} = a\rho\vec{\nabla}\rho - \vec{F}_{ext}\rho, \tag{5.43}$$

where the constrains imposed by the wall render the density flux, $\vec{j}$, zero. The problem is quasi one dimensional since the dependencies are all along the x-direction. We set periodic boundary conditions along the y-direction to minimize the confinement in this direction. The expression for the density profile inside the channel is then

$$\rho(x) = \frac{F_{ext}}{a}(x - x_0) + \rho(x_0), \tag{5.44}$$

where x_0 is the point along the channel at which the density becomes zero, and therefore, $\rho(x_0) = 0$. The linear dependence on x can be used to calculate the parameter of interaction from the simulations and compare it with the theoretical result. We can see from Fig. 5.3, which shows the density profile of a simulation in the stationary state, that there is a deviation from the linearity near $x = 0$ which comes from the interaction with the wall. We have tried the Yukawa, hard wall and the harmonic potentials as wall interactions with different parameters, but the deviation is always present. We chose a suitable arrangement that prevented the wall from interacting with many particles. Using only data from regions that are not significantly affected by the wall, we calculated

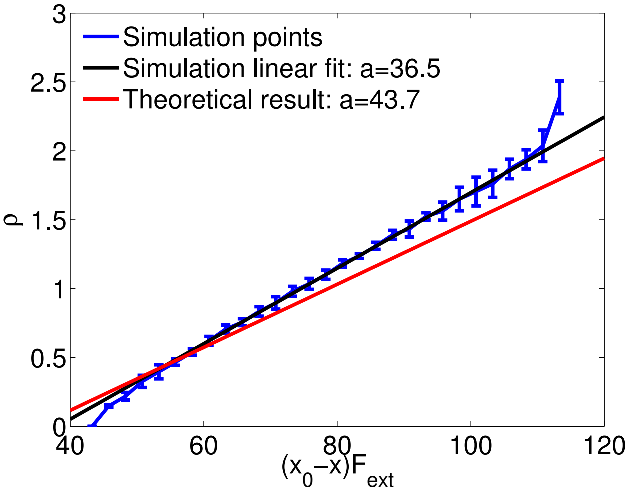

FIGURE 5.4: Estimation of the interaction parameter for the system shown in Fig. 5.3. The blue line is the numerical data averaged over ten samples, the black line is the optimal linear fit to the data and the red line is the expected theoretical result.

the slope of the best linear fit to the density profile, to estimate the numerical value of a.

The result achieved by averaging ten samples in Fig. 5.3 can be seen in Fig. 5.4. The black line shows the fit to the numerical data and the red line the result expected from the theory. The theoretical prediction is overestimated. We preformed the same calculation for different V_0, α, particle number and external forces and the interaction parameter calculated from the simulations is in all cases $\sim 15\%$ smaller than the one from the theoretical model.

To confirm that this discrepancy was not a result of errors in the code, we also made the channel test with LAMMPS, a package commonly used by the scientific community to preform molecular dynamics. The results achieved were identical to the ones of the developed code.

While the qualitative behavior was well captured, the theoretical model predicts a higher repulsion between particles than the one we calculate in the simulations. The deviation is a consequence of the truncation done in the expansion of the density, in both derivations we assumed that the density is a smooth function in space. The interaction parameter reflects this choice by forcing the density to spread by increasing the repulsion between particles. A simple illustration of this effect can be seen by rearranging Eq. (5.43)

$$\vec{F}_{ext} = a\vec{\nabla}\rho, \tag{5.45}$$

where the external force is constant. If the theoretical density is smoother than in the simulations, the magnitude of the gradient is lower and a is higher to balance it.

In reference [58] the authors discuss that the parameter a is only valid for an unconfined system, since it only depends on the interaction potential, and they show that its magnitude increases when the confined system decreases its size.

Chapter 6

Self-assembly driven by a periodic stationary field

In this chapter, we use a space periodic field to drive the colloidal particles. For simplicity, we consider only repulsive interactions ($V_0 > 0$). The interaction parameters a and A are identical for the Yukawa potential, and hereafter, we use only the A notation to refer to the interaction parameter. In the numerical simulations we set $\alpha = 1/2$ and change A by varying V_0.

In a physical system colloids can be driven by electric fields. However, the ions and counter ions that compose the fluid also interact with an electric field and some non-trivial effects that we did not consider in the model can arise. Our model is more appropriate to describe the interaction with a magnetic field that drives the particles without prompting a new fluid/field interaction. In this case, the particles move according to the gradient of a non-uniform magnetic field, in a process commonly referred to as magnetophoresis. The quantity that is equivalent to the charge in an electric interaction is, this time, the difference between the magnetic susceptibilities of the particles and fluid.

We consider an external field that is constant along the y-direction and periodic along the x-direction. The particle/field interaction in our model is described by a periodic potential,

$$V_{ext}(x, y) = V_{ext}(x) = V_E \sin(\kappa x), \tag{6.1}$$

where V_E is the strength of the potential and

$$\kappa = \frac{2\pi P}{L} \tag{6.2}$$

is the wave number. P sets the number of minima of the potential.

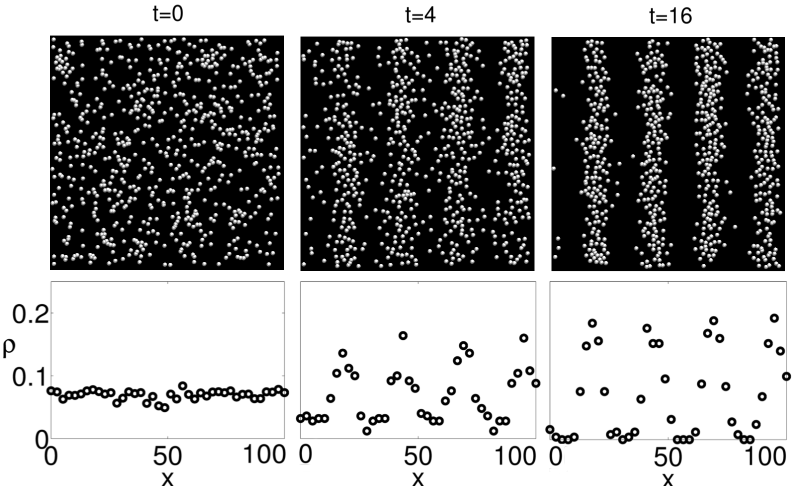

FIGURE 6.1: Snapshot of the system for $t = 0$, $t = 4$ and $t = 16$. The plots correspond to the density profiles along the x-direction. Under the influence of the external potential the particles organize into bands. The linear length of the system is $L = 100$, the interaction parameters are $V_0 = 5$ and $\alpha = 1/2$. The strength of the field is $V_E = 5$ and the number of minima is $P = 4$.

We start our simulations with a uniform (random) distribution of colloidal particles and switch on the field at $t = 0$. The simulations were performed inside square boxes of three different linear lengths $L = \{100, 120, 150\}$, in units of the particle radius. By fixing the density $\rho = 0.0696$, we simulate $N = \{696, 1000, 1560\}$ colloidal particles, respectively.

6.1 Results

In the absence of external fields the spatial distribution of the colloidal particles is homogeneous. When the external field is switched on the particles are dragged towards the closest minimum and self-organize into individual bands around it (see snapshots in Fig. 6.1). To quantify the spatial arrangement of the colloidal particles we measure the density, $\rho(\vec{r})$, defined as the number of particles per unit area. Given the symmetry of the external field (see Eq. (6.1)), we focus on the profile of the density along the x-direction. Figure 6.1 shows a snapshot and the density profile for a system with $L = 100$ at three different times. The density profile has the symmetry of the external potential. The maxima of the density correspond to the minima of the potential. Similarly, the density vanishes at the maxima of the potential. We run the simulations for 6×10^6 timesteps. After this time, the changes in the density profile are within the error bars and thus we consider that the stationary state has been reached. Simulations with different system sizes were preformed and we found no significant finite-size effects.

The collective dynamics and the band structure result from a complex interplay of the particle/fluid, particle/field and particle/particle interactions. Here, we analyze how

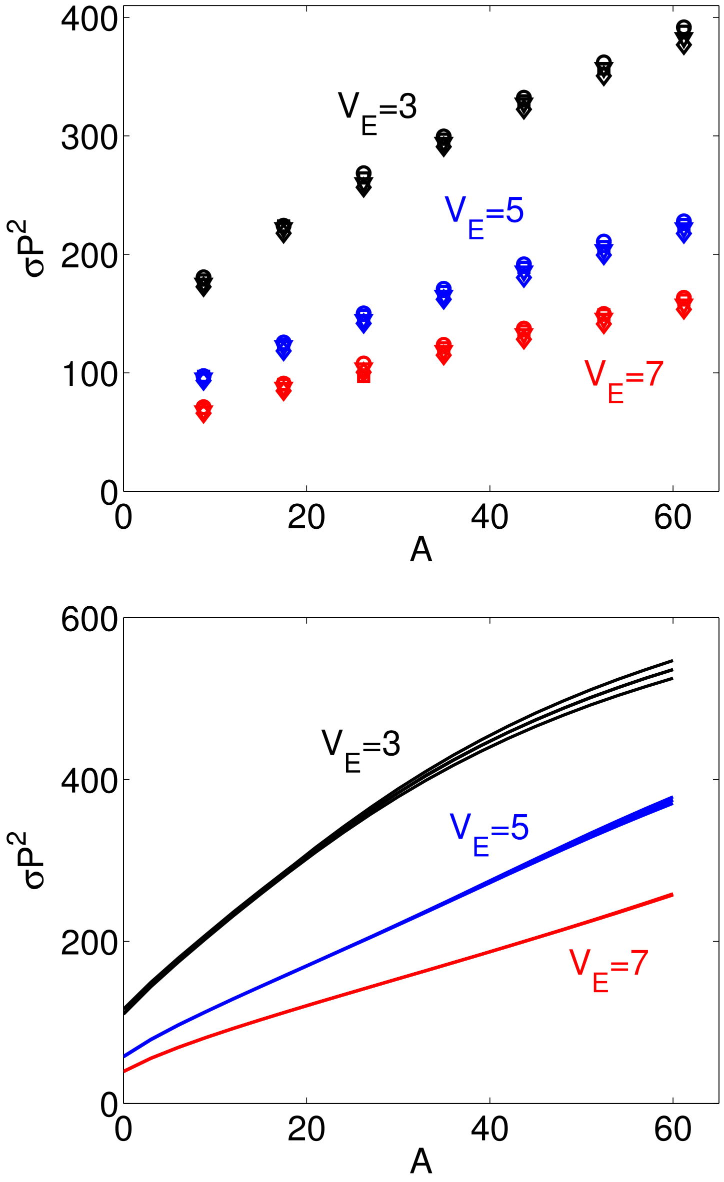

FIGURE 6.2: Mean square displacement of the particle position around the potential minima. On the left-hand side are the results obtained from the Brownian dynamics simulations and on the right-hand side those from the DFT calculations. The data is obtained by averaging over 25 samples rescaled by P^{-2}. Black, blue and red represent respectively $V_E = \{3, 5, 7\}$ and the circle, square, triangle and diamond symbols correspond respectively to $P = \{1, 2, 3, 4\}$. The error bars are smaller than the size of the symbols. The particle/particle and particle/field interactions have opposite effects on the final configuration. While the former promotes wider bands the latter favors thinner ones.

the final structure and dynamics depend on the model parameters. We start with an analysis of the stationary state and proceed with the study of the dynamics.

6.1.1 Stationary state

6.1.1.1 Numerical simulations

We first characterize the stationary state that corresponds to the thermodynamic equilibrium configurations. For $P > L/2$ the average particle/field interaction vanishes, as the wave length of the potential is shorter than the particle diameter. The limit of no external field is then recovered. For $P < L/2$ and strong enough field, particles accumulate around the minima forming a band structure. Thermal noise and particle/particle interaction cause a broadening of the bands, giving them an effective thickness. This thickness is a property of the equilibrium configuration. To quantify it, we measure the mean square displacement of particles around the local minimum

$$\sigma = \langle x_b^2 \rangle - \langle x_b \rangle^2 \tag{6.3}$$

where the average is over particles in the same band, i.e., in between two consecutive maxima of the potential. x_b is their position relative to the local minimum along the x-direction. The average displacement is zero as the distribution of particles is symmetrical with respect to the center of the band (minimum of the potential).

Figure 6.2 (left panel) shows the dependence of σ on the model parameters. One clearly sees that, for a given thermostat temperature, the thickness of the bands results from the competition between particle/field and particle/particle interactions. The particle/field interaction promotes the formation of thin bands. The stronger the field (V_E) the thinner the band is. By contrast, the particle/particle repulsion tends to homogenize the spatial distribution of the particles and favors wider bands. Consequently, σ increases monotonically with A. Note that when we rescale σ by P^2 a data collapse is obtained for different P values into a single curve that depends only on V_E and A. In the next section we perform a density-functional theory (DFT) analysis to study these dependences.

6.1.1.2 Density-functional theory analysis

Figure 6.3 shows the density profile obtained from numerical simulation and DFT for the same set of parameters. The DFT results deviate from the simulation only at the maximal and minimal densitities. The maximal density is underestimated and the minimal is slightly overestimated. We evaluated how this deviation depends on the model parameters. Figure 6.4 shows the dependence on A of the maximal density ρ_{max}, defined as the density in the center of the band, for different values of V_E and P. We find that, while the deviation of the DFT calculation from the simulation increases slightly

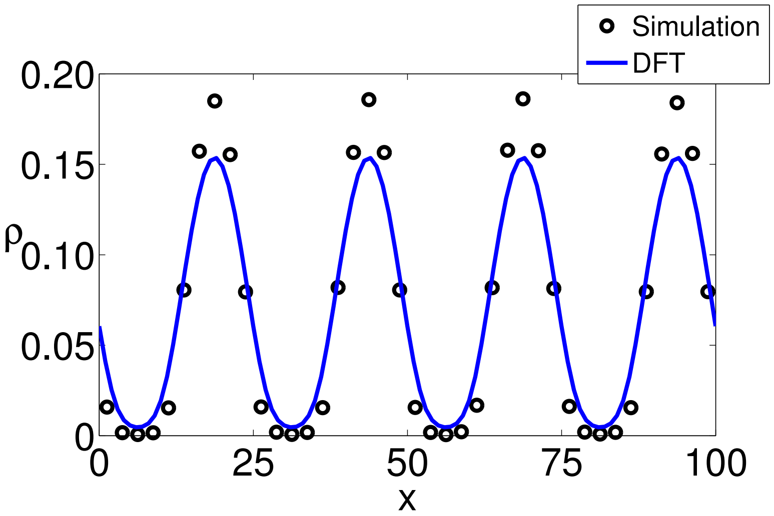

FIGURE 6.3: Density profile for $L = 100$, $V_E = 5$, $A = 43.71$ and $P = 4$. The dots are the numerical results obtained by averaging over 100 samples and the line is the result of DFT. The theory is in good agreement with the simulations but it underestimates the density at the maxima.

with A it does not vary significantly with V_E and P. This also leads to theoretical values of the mean square displacement σ, which are larger than those obtained by simulation. However, as shown in Fig. 6.2 (right panel) one recovers the same qualitative dependence on the model parameters and the values of σ are of the same order of magnitude.

Since the density profile is symmetric with respect to the center of the band, the mean square displacement is given by,

$$\sigma = L \int_{-\frac{L}{2P}}^{\frac{L}{2P}} x^2 \rho^*(x) dx. \tag{6.4}$$

where $\rho^*(x) = \rho(x) N_b^{-1}$ is the probability density function for particles in the band and $N_b = L \int_{-\frac{L}{2P}}^{\frac{L}{2P}} \rho(x) dx$. The L outside of the integral accounts for the integration of the domain along the y-direction. Assuming that $\rho(x)$ is constant and $N_b = N/P$,

$$\sigma = \frac{L^2}{12P^2} \quad . \tag{6.5}$$

Thus, $\sigma \sim P^{-2}$ as observed both from the simulations and the DFT analysis. Note that the maximal density (in Fig. 6.4) does not depend on P. From Eq. (5.11) we also conclude that, near the minima, the external potential and the interaction terms have different signs. Consequently, V_E and A have opposite effects on σ, as observed in the simulations and DFT calculations, see Fig. 6.2.

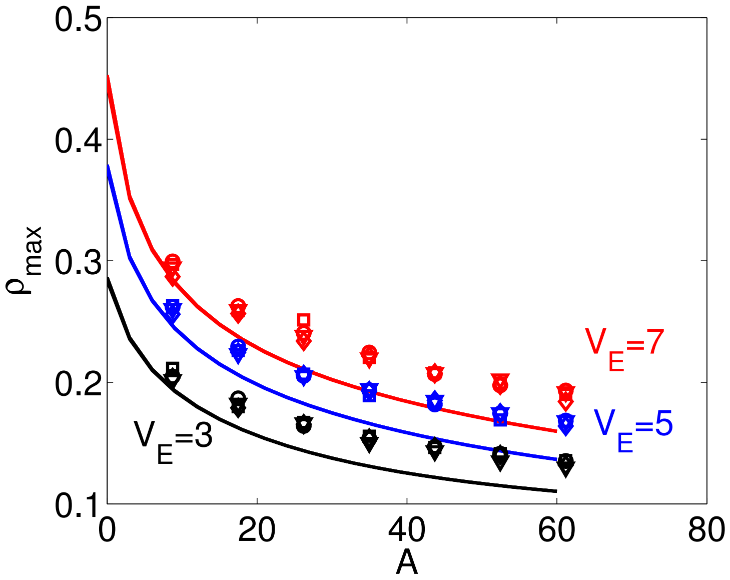

FIGURE 6.4: Maximum density of the profile. Each data point is an average over 25 samples and the lines are the DFT results. Black, blue and red represent respectively $V_E = \{3, 5, 7\}$ and the circle, square, triangle and diamond symbols correspond respectively to $P = \{1, 2, 3, 4\}$. The error bars are smaller than the size of the symbols. Note that the density does not depend on P. The deviation of the theoretical curves from the simulation results increases particle interactions increase. The effect of A and V_E on the maximal density is opposite to their effect on the mean square displacement.

By taking the logarithm of Eq. (5.11) we obtain

$$\log(\rho(x)) + \beta A\rho(x) = log(Z) - \beta V_E sin(\kappa x). \tag{6.6}$$

The dependence of the first term of the left-hand side on the density can be neglected with respect to the second term in two limiting cases: for strong particle/particle interactions or high enough densities. In the former, the strong particle/particle repulsion hinders the formation of bands and homogenizes the density. The external potential acts as a perturbation to the uniform distribution of particles, which is sinusoidal in space and linear on V_E. The contributions from the external potential and particle interactions are given by $\rho(x)$ which means that the dependence of the mean square displacement on the strength of the potential intensity is the same in both limits, as seen in Fig. 6.5(a) and (b). For weak particle interactions the curves are linear when the strength of the potential is also small. But as the particle/particle interaction increases, the potential intensity where the dependence deviates from linear also increases. Note that the curve for $A = 0$ corresponds to the ideal gas where the dependence of $\rho(x)$ on the strength of the potential is exponential as expected from Eq. (5.11). For $V_E = 0$ the density is uniform and the value of σ is given by Eq. (6.5) and is the same for all curves.

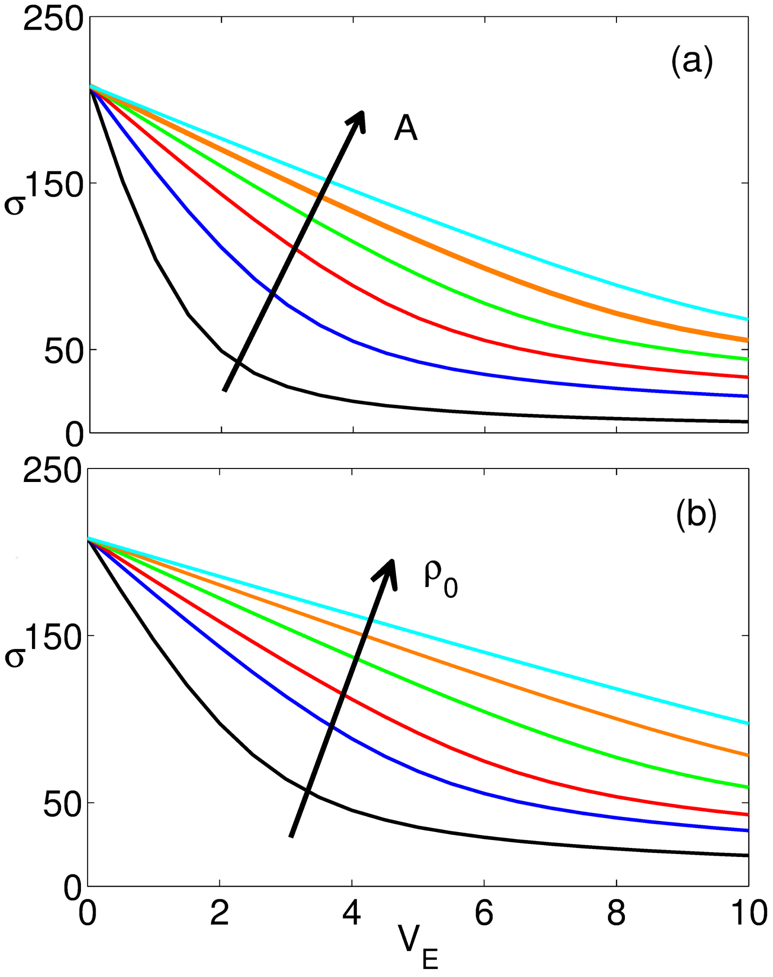

FIGURE 6.5: DFT results for the mean square displacement for $P = 2$. The lines in (a) are for $A = \{0, 20, 40, 60, 80, 100\}$ and the lines in (b) are for different initial densities $\rho_0 = \{2.50, 6.96, 10.0, 15.0, 20.0, 25.0\} \times 10^{-2}$. For strong inter-particle interactions and weak external potentials the dependence is linear in V_E. The linear dependence is also observed at high densities.

6.1.2 Relaxation dynamics

6.1.2.1 Numerical simulations

We analyze now the relaxation towards the stationary state shown in Fig. 6.1. Namely, we investigate how the relaxation time depends on the model parameters.

We start with a uniform spatial distribution of particles, $\rho(x) = \rho_0$. As the external potential is switched on the colloidal particles move accordingly and regions of high density of colloids are formed (bands). For a systematic analysis, we focus on the evolution of the positions of the minima, ρ_{min}, corresponding to the potential maxima, and the positions of maxima, ρ_{max}, corresponding to the potential minima. Figure 6.6

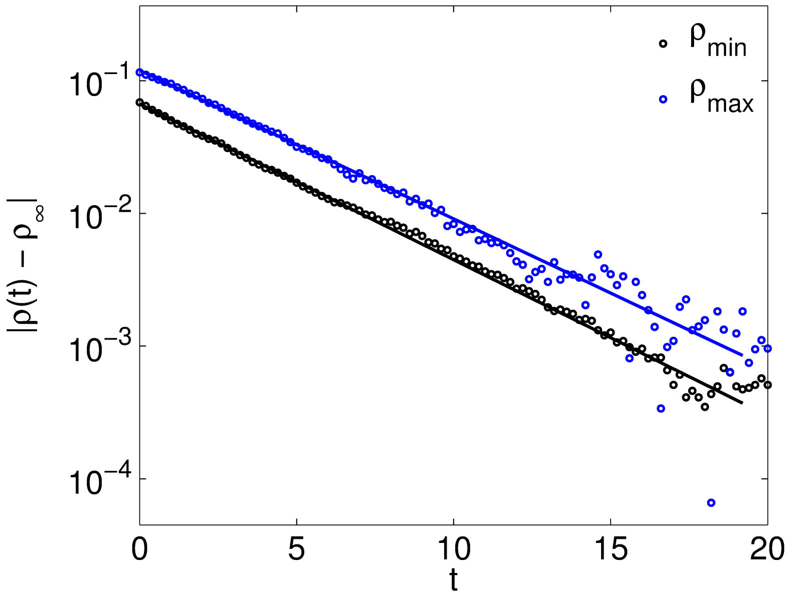

FIGURE 6.6: Evolution of the maximal and minimal densities. The relaxation into the stationary state is exponential. The scattered data are the numerical results and the lines the exponential fitting. The results shown are averages over 100. The parameters are $L = 100$, $V_E = 5$, $A = 43.71$ and $P = 4$.

shows the convergence of these densities to their value in the stationary state, ρ_∞, for a particular set of parameters. One clearly sees an exponential decay in time.

We define the relaxation time τ^{relax} as the inverse of the slopes of the evolution curves. Figures 6.7 and 6.8 show that the dependence on the model parameters is different for the minima and the maxima suggesting that the underlying relaxation mechanisms are different. In general, strong potentials favor short relaxation times while the dependence on the particle/particle interaction is not straightforward. Also, data collapse is observed when we rescale τ with P^2. We will now use DDFT to shed light on these findings.

6.1.2.2 Dynamic density-functional theory analysis

We focus on the maximal and minimal densities where $\vec{\nabla}\rho = 0$. Let us assume that $\nabla^2\rho = \rho_2$ is constant in time at these points. At the minimum $\rho_2 \geq 0$ and at the maximum $\rho_2 \leq 0$. By solving Eq. (5.13) we get

$$\rho_{\substack{min\\max}}(t) = -\frac{k_B T \rho_2}{A\rho_2 \mp V_E \kappa^2} + K_1 \exp\left[\frac{A\rho_2 \mp V_E\kappa^2}{\gamma} t\right], \tag{6.7}$$

where the expression with the minus sign is for the density at the minimum and the plus sign for the density at the maximum. By fixing the initial density it is possible to calculate the constant

$$K_1 = \frac{N}{L^2} + \frac{k_B T \rho_2}{A\rho_2 \mp V_E \kappa^2}. \tag{6.8}$$

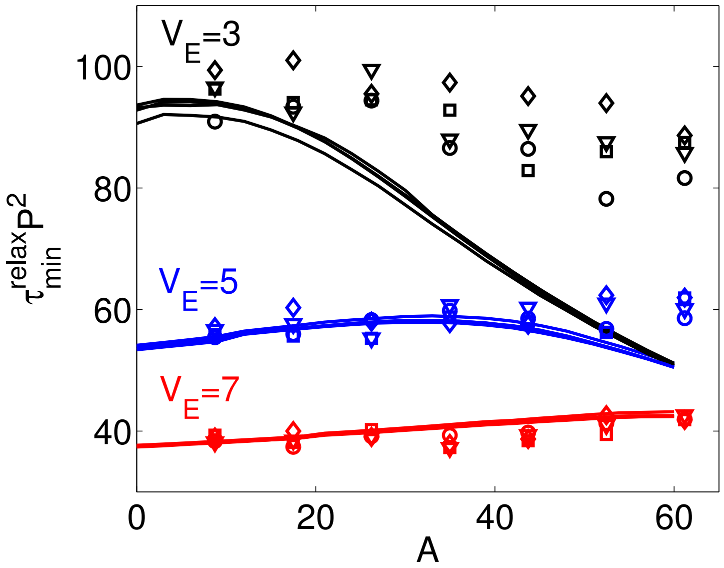

FIGURE 6.7: Relaxation time of the minimal density. The scattered data are the simulation results and the solid lines the ones from the DDFT calculations. Black, blue and red represent respectively $V_E = \{3, 5, 7\}$ and the circle, square, triangle and diamond symbols correspond respectively to $P = \{1, 2, 3, 4\}$. The simulation results are averages over 45 samples for $V_E = 3$ and 25 samples in the other cases. The relaxation time does not vary monotonically with the interaction strength. It exhibits a maximum that depends on the balance between A and V_E. The relaxation time is proportional to P^{-2}.

If we define the characteristic relaxation time as

$$\rho(t) - \rho_\infty \sim e^{-t/\tau^{relax}} \tag{6.9}$$

where ρ_∞ is the density at the given point at equilibrium, we arrive at the following expression

$$\tau^{relax}_{\substack{min\\max}} = -\frac{\gamma}{A\rho_2 \mp V_E\kappa^2}. \tag{6.10}$$

In the region of parameters where $\nabla^2\rho = const$ the relaxation time is inversely proportional to A and V_E. The friction coefficient also plays a role on the dynamics and the relaxation time is a monotonic increasing function of the viscosity. Replacing κ using Eq. (6.2) we conclude that $\tau^{relax} \sim P^{-2}$. The relaxation time decreases with the number of bands as, on average, particles have to travel a shorter distance to reach the nearest potential minimum. Eq. (5.13) is solved numerically using first order finite elements in the 2D square domain with periodic boundary conditions [59]. Figures 6.7 and 6.8 show the relaxation time of the minimal and maximal densities, respectively. They collapse for P^{-2} but the inverse proportionality is only observed for high A which is where our approximation holds.

The theoretical results underestimate the relaxation time by comparison with the data

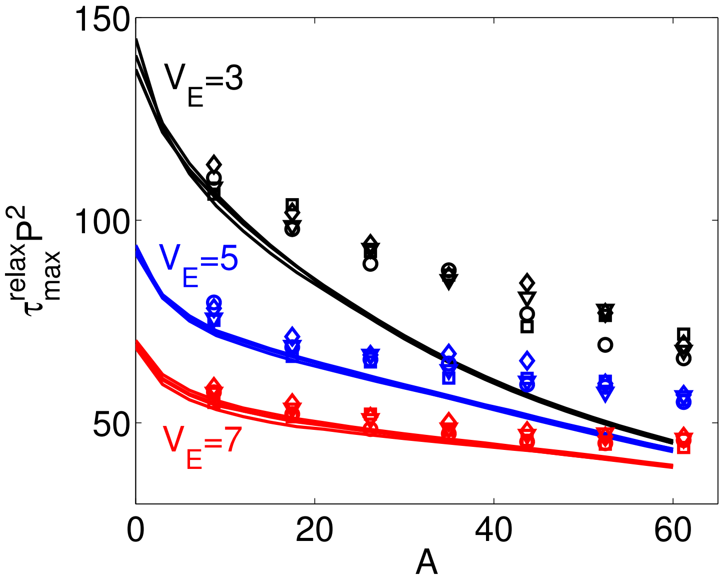

Figure 6.8: Relaxation time of the maximal density. The scattered data are the numerical results and the solid lines the ones from the DDFT calculations. Black, blue and red represent respectively $V_E = \{3, 5, 7\}$ and the circle, square, triangle and diamond symbols correspond respectively to $P = \{1, 2, 3, 4\}$. The simulation results are averages over 45 samples for $V_E = 3$ and 25 samples in the other cases. For strong interparticle interactions the relaxation time depends weakly on the external potential.

from the Brownian dynamics simulations, consistent with the fact that DDFT overestimates the diffusion coefficient [55]. The deviation is greater at low V_E and high A, when the particle/particle interactions dominate the dynamics. Recall that the term for particle/particle interaction in Eq. (5.6) is the only approximate term.

Note that the relaxation time is always positive. For the minimal density the curvature ρ_2 is typically small and the external potential term dominates. For the maximal density the curvature is negative and the particle/particle interaction term dominates over the external potential. In the minimum the particles try to escape and so the external potential is the relevant interaction leading to a decrease in the density. However, the process is still influenced by the presence of neighboring particles and the relaxation time increases with A at low A, Fig. 6.7. For strong interparticle repulsions there is a broadening of the bands; the particles will then travel shorter distances to reach their equilibrium positions, decreasing τ^{relax} at the minimal density. By contrast, for the maximal density the repulsions strongly affect the dynamics.

The relaxation times obtained from the simulations and the theory coincide for strong potentials as the effect of the interparticle interactions is irrelevant. When V_E decreases the particle/particle repulsion becomes relevant and the LDA approximation leads to increasing deviations from the simulation results. Equation (6.10) suggests that for high enough values of A the relaxation times do not depend on V_E and P and converge to the same value in line with the results shown in Figs. 6.7 and 6.8. For lower A at the maxima, where the particles are compressed, equilibrium takes longer to be reached.

Chapter 7

Self-assembly driven by a time varying field

In this chapter we analyze a colloidal dispersion under a time varying external field. Once again, we consider a two dimensional system, with periodic boundary conditions. There are now two types of particles present, A and B, with opposite charges. Both types are in equal number and, since A and B have opposite charges, the force resulting from the interaction with the field is applied in opposite directions for each type. The system consist of $N = 5000$ particles and it has linear size $L = 145$. We set the integration timestep to $\Delta t = 10^{-5}\tau$.

For simplicity, we neglect the charge difference in the particle/particle interactions in our main analysis. Instead, the interaction is always repulsive and characterized by the Yukawa potential with $V_0 > 0$. We are focus on the limit in which the external field is the main element that drives the evolution and the charge is sufficiently low to neglect particle/particle attractive interactions.

The field is uniform in space but rotates counter-clockwise with constant angular velocity ω that is expressed in units of τ^{-1}. Specifically,

$$\vec{E}_{ext} = E\left[\cos\left(\omega t\right)\hat{x} + \sin\left(\omega t\right)\hat{y}\right], \tag{7.1}$$

where E is the magnitude of the field, expressed in units of $\frac{V_0}{|q| r_p}$, where $|q|$ is the unit charge. Depending on its type, a particle i can have charge $q_i = \pm 1$.

Before we apply a rotational field at $t = 0$, we start with a random distribution of particles and apply a uniform external field ($\omega = 0$) for τ.

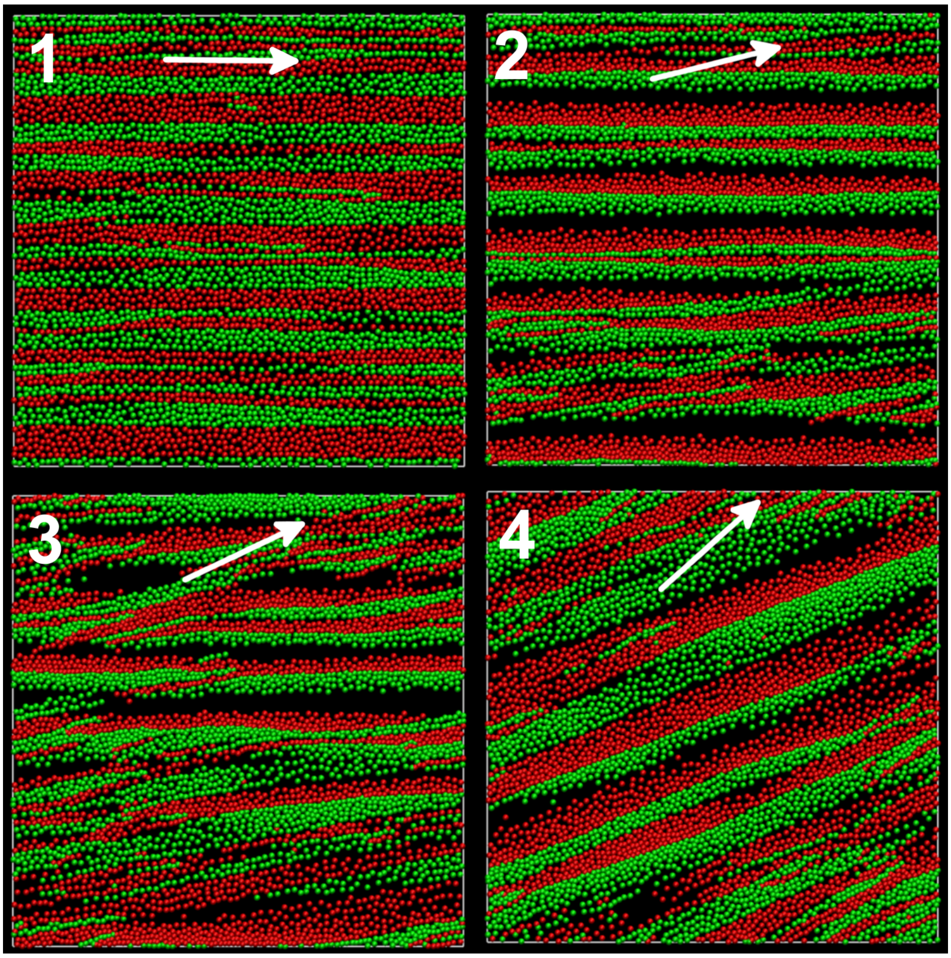

FIGURE 7.1: Snapshots of the system at $t = 0$ (in 1), $t = 0.25$ (in 2), $t = 0.45$ (in 3) and $t = 0.75$ (in 4), with $\omega = 0.8$ and $E = 1.6$. The white arrows represent the direction of the external field at each time.

7.1 Results

When only subject to a constant field, the particles of positive charge will move in the field direction (type A, green in Fig. 7.1) and the others in the opposite direction (type B, red in Fig. 7.1). The particles in the counter flow suffer repeated collisions and will eventually organize into lanes of particles of their own type, has can be seen in snapshot 1 in Fig. 7.1, where the lanes are horizontal. This is a steady-state that is characterized by a constant flux of type A and another of type B, equal in magnitude but with opposite directions. Our goal is to study the stability of these kinetic structures under a rotating electric field.

In Fig. 7.1, snapshot 2, the field already has a vertical component forcing the particles to move accordingly in that direction. However, the neighboring lanes composed by opposite charged particles create obstacles to the motion along the vertical direction. The particles are compressed in an interface between two lanes, leaving available space

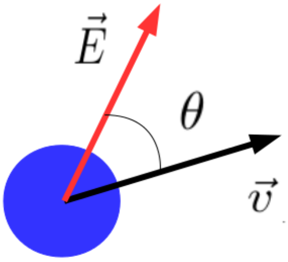

Figure 7.2: The shift θ is the average over all particles of the angle between the directions of the field and the velocities of the particles. This picture represents the shift for a type A particle. For the type B we need to subtract π to the shift since their velocity points in the opposite direction.

behind. When the component of the field that is perpendicular to the lane direction increases, the interfaces disrupt creating bursts of particles that interfere with other lanes, potentially destabilizing their interface. Eventually, the system rearranges completely forming new lanes with a orientation that is closer to the direction of the field (snapshots 3 and 4 from Fig. 7.1).

To characterize the stability of the lanes we define the shift θ as the average of the angle between the directions of the field and the velocity of the particles (see Fig. 7.2). When $\theta \approx 0$, the particles are moving in the direction of the field on average. When the shift increases, the system is trapped in a lane configuration where the particles are forced to move in the direction of the lane.

The evolution of the shift resulting from the averaging of fifteen samples with $\omega = 0.1$ and $E = 0.8$ is shown in the top plot in Fig. 7.3. The initial lane configuration withstands the rotation of the field for $t \sim 3.5$ causing the first shift increase. From that point, the interfaces that hold the structure are broken and the particles move in the direction of the field, drastically decreasing the shift. The subsequent peaks mark new stable lane configurations.

It is noteworthy that the shift peaks are so well defined, showing that for low ω there is consistency of the results over different samples. The lanes are being formed and destroyed at approximately the same times. The periods involved in lane formation and destruction largely depend on the parameters of the field. In fact, lane stability is a consequence of the interplay between ω and E. While the rotation causes lane destruction, the intensity of the field promotes lane stability. The latter is expected since particle/particle collisions is the mechanism behind the lane formation, increasing their intensity at the interfaces (by increasing the magnitude of the field) should promote more resilient lanes.

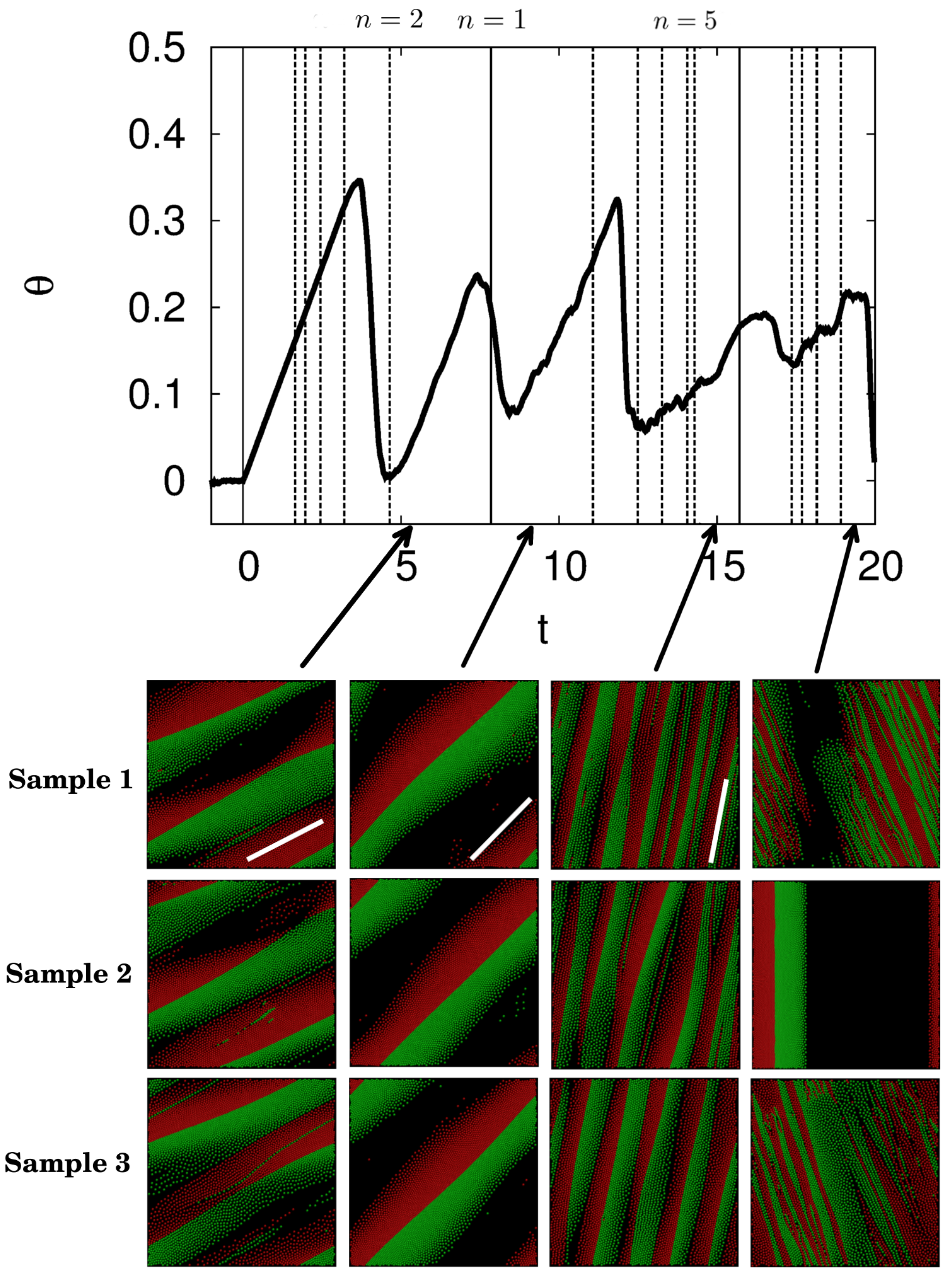

FIGURE 7.3: Evolution of the shift θ for an external field with $\omega = 0.1$ and $E = 0.8$. The result is an average over fifteen samples. The vertical solid lines indicate, from left to right, the time at which the angle of the external field is $\theta_E = \left\{0,\ \frac{\pi}{4},\ \frac{\pi}{2}\right\}$ that correspond to wrapping numbers $n = \{\infty,\ 1,\ \infty\}$, respectively. The dashed vertical lines are the times at which the external field angle is equal to a magic angle, Ψ. Only the magic angles that correspond to wrapping numbers from one to six are shown, but there are infinite magic numbers that approach $\Psi = 0$ and $\Psi = \frac{\pi}{2}$ from both sides with increasing wrapping numbers. Four snapshots of the system from three different samples are shown at the bottom, and the white bars show the magic angle of lane arrangement, $\Psi = \{0.4636, 0.7854, 1.3734\}$ with $n = \{2, 1, 5\}$ from the first to the third time.

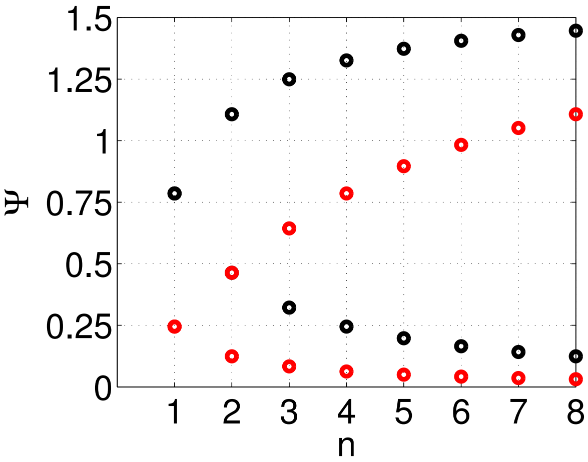

FIGURE 7.4: Magic angles at which a lane can be orientated in a system with periodic boundary conditions. The black circles are for $\frac{L_x}{L_y} = 1$ and the red circles for $\frac{L_x}{L_y} = 4$.

In Fig. 7.3 we also show snapshots of the system for three different samples. The first three snapshots were taken during periods in which the particles are trapped in a lane configuration (the shift is increasing). The state of the system is identical in all samples, there is only one lane of type A and another of type B that wrap the system (there is a fixed number of wraps at each time). These lanes are oriented at the same angle in every sample. The fact that these three cases have such similar configurations during the evolution is a direct consequence of the use of periodic boundary conditions.

There is an integer number of times a lane can wrap inside a finite system with periodic boundary conditions and the angles at which they can span from one side of the system to the other are quantized. We call these the magic angles, Ψ. Each one is associated with a wrapping number, n. They only depend on the geometry of the system and their values for a general rectangle are given by

$$\begin{cases} \frac{L_y}{L_x} = n\tan(\Psi) & \text{, for } k\frac{\pi}{2} \leq \Psi \leq \arctan\left(\frac{L_y}{L_x}\right) + k\frac{\pi}{2} \\ \frac{L_x}{L_y} = n\cot(\Psi) & \text{, for } \arctan\left(\frac{L_y}{L_x}\right) + k\frac{\pi}{2} < \Psi \leq (k+1)\frac{\pi}{2}, \end{cases} \tag{7.2}$$

where L_x and L_y are the orthogonal sizes of the rectangle and $k = 0, 1, 2, 3, ...$ The formula is valid for $L_x \geq L_y$. Figure 7.4 shows the magic angles for $\frac{L_x}{L_y} = 1$ (in black) and $\frac{L_x}{L_y} = 4$ (in red). With the increase of the wrapping number, the magic angles get closer to each other and they enter a quasi-continuum region towards the limits $k\frac{\pi}{2}$ (corresponding to $n = \infty$).

The angle of the external field is given by $\theta_E(t) = \omega t$ (which is a way of measuring the time in units of ω^{-1}). The vertical lines in the top plot from Fig. 7.3 are the times at which $\theta_E = \Psi$ for the wrapping numbers with $n = \{1, ..., 6 \text{ and } \infty\}$ as predicted from Eq.

(7.2). The first shift peak shows that the system is not rearranged every time θ_E is equal to a magic angle. Lanes are structures that resist reorientation. When they are finally destroyed, we see that the angle in which the new configuration is trapped corresponds to the closest magic number at the time the system is rearranging, i.e., when the shift drops. This is clear from the first two snapshots. The third one is at a moment in time in which the shift peaks are not so well defined because θ_E is crossing consequent magic numbers, corresponding to high n, in a rapid succession while it approaches $\theta_E = \frac{\pi}{2}$. During this period the system can almost gradually change from one configuration to the next, since the magic angles are very close in value.

The fourth snapshot in Fig. 7.3 shows that samples one and three are already rearranging in configurations with $\Psi > \frac{\pi}{2}$, while sample two is still in the configuration with $\Psi = \frac{\pi}{2}$, that is equivalent to the initial state. The magic angle cycle is repeated every $\frac{\pi}{2}\omega^{-1}$ time periods.

Figure 7.5 shows that the orientation of the lanes in a rectangle system with $\frac{L_x}{L_y} = 4$ also follows the magic angles (their values are given by the red data from Fig. 7.4). Some tests were done for systems with different sizes and particle densities and we found that lanes are always arranged according to one magic angle.

Figure 7.6 shows the shift evolution for the parameters $\omega = 0.6$ and $E = 2$, the vertical lines limit the magic angle periods. Once again, one finds well defined peaks, but now the dynamics are faster and the evolution exhibits periodicity (with the period of Ψ). The distinctive features in the beginning show that the initial configuration only affects the evolution in the first period.

For high ω the lanes still arrange according to the magic angles given by Eq. (7.2), but they do it at different times and orientations in every sample. The shift peaks disappear with the averaging and its evolution fluctuates around a constant value, which is an evidence of the chaotic nature of the process of lane formation in these regimes. The top panel from Fig. 7.7 shows the shift evolution for one sample and it reveals that lanes are formed at irregular times.

The system is in the stationary state (albeit far from equilibrium) after the first magic angle period. We show the shift time average of the remaining of the evolution in Fig. 7.8 for different field parameters. The average shift in the stationary state increases with ω since the adjustment of the particles trajectory to the direction of the field is slower than ω. The increase of the field intensity has the opposite effect on the average shift. We commented before that the field intensity promotes the stability of the lanes (increasing the shift), but it happens that for strong fields they also take longer to form.

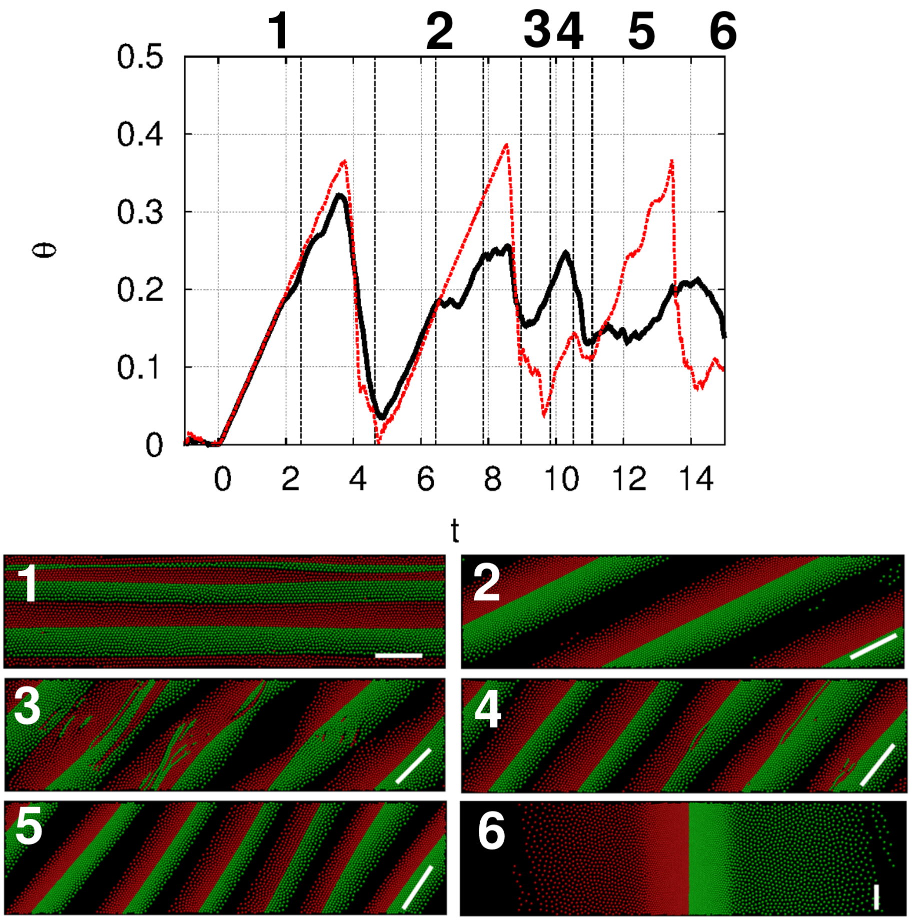

FIGURE 7.5: The top plot shows in solid black the evolution of the shift θ for an external field with $\omega = 0.1$ and $E = 0.8$ in a system with $\frac{L_x}{L_y} = 4$. The result is the average over five samples. The dashed vertical lines are the times at which the external field angle is equal to a magic angle, Ψ, for $n = \{1, 2, 3, 4, 5, 6, 7, 8\}$. The dashed red line shows the shift evolution of one single sample. Six snapshots of this sample are shown for the times $t = \{1.75, 6.28, 9.3, 10.4, 12.0, 19.0\}$, indicated by the bold numbers on the top. The lane arrangement at each time follows the magic angles $\Psi = \{0, 0.4636, \frac{\pi}{4}\, 0.8961, 0.9828\frac{\pi}{2}\}$ with $n = \{\infty, 2, 4, 5, 6, \infty\}$, respectively. The white bars show the orientations of Ψ.

The system is most of the time in the disordered state which decreases the shift time average (see top panel of Fig. 7.7).

In previous works on the lane formation [36, 60] under an uniform external field, it was common to use a parameter ϕ, that measures the segregation of particles in the system and is defined as

$$\phi = \frac{1}{N} \sum_i \frac{(n_{li} - n_{oi})^2}{(n_{li} + n_{oi})^2}, \tag{7.3}$$

where n_{li} and n_{oi} are respectively the number of like and opposite charged particles within a radius $r = 8$ of particle i. This parameter is 1 when the system is completely segregated and 0 when completely mixed.

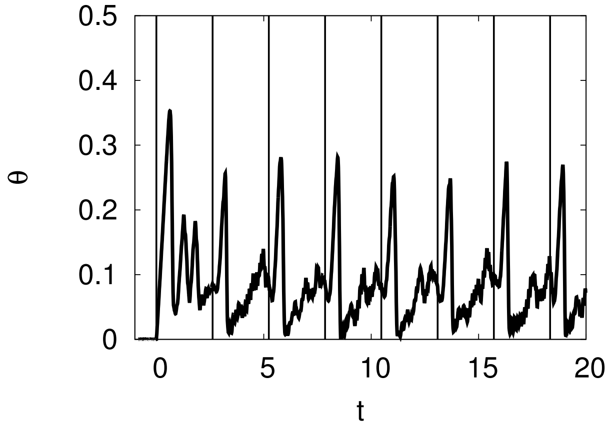

FIGURE 7.6: Shift averaged over fifteen samples for a system with $\omega = 0.6$ and $E = 2$. The vertical lines are the times at which $\theta_E = k\frac{\pi}{2}$.

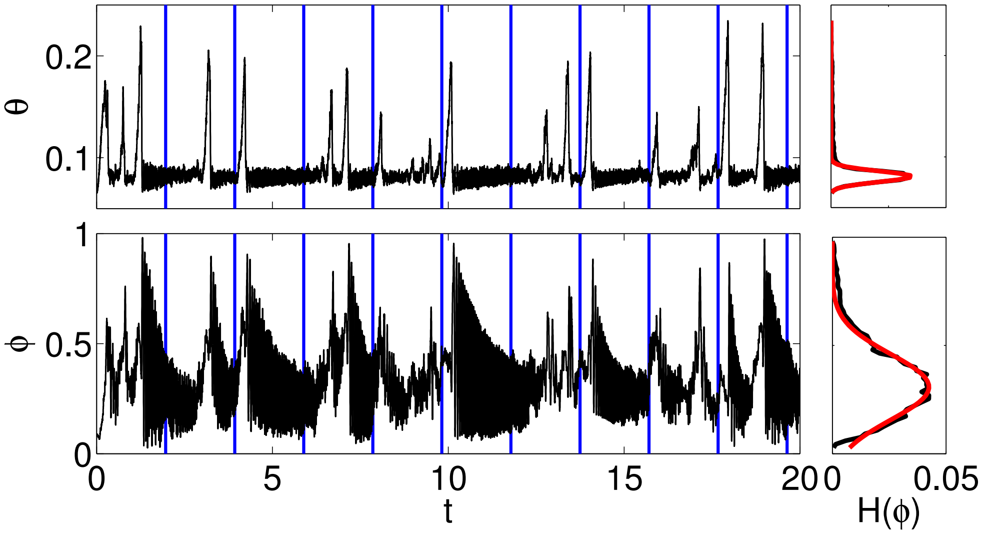

FIGURE 7.7: Shift (top) and segregation (bottom) parameter evolution of one sample with $\omega = 0.8$ and $E = 2$. On the right it is plotted the point distribution of both evolutions in black and the Gaussian fit in red. The blue lines indicate the times at which $\theta_E = \frac{\pi}{2}\omega^{-1}$

In Fig. 7.9 we show the time average of the segregation parameter in the stationary state. It decreases with the rotational velocity and increases with the field magnitude. The bottom panel of Fig. 7.7 shows that lane formation causes particle segregation, $\phi \sim 1$ when the shift peaks, and ϕ oscillates rapidly in the periods between lane states.

Except for showing that lane states correspond to periods of high segregation this parameter does not prove to be particularly useful in the analysis of the rotational system.

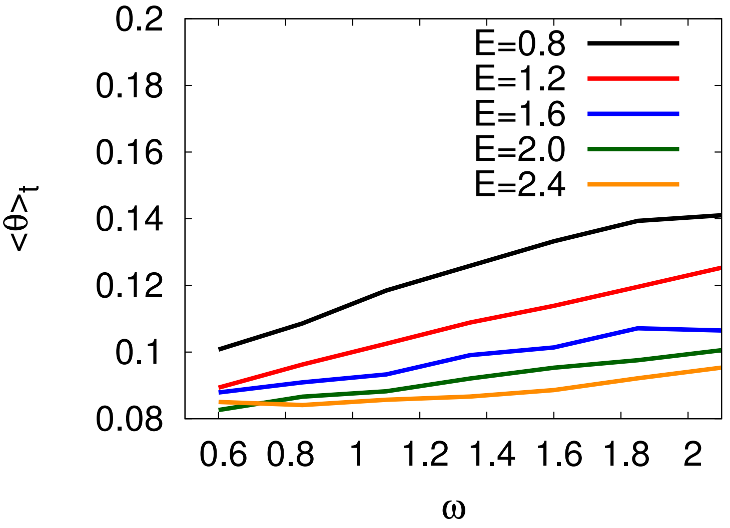

FIGURE 7.8: Time average of the shift between the direction of the external field and the orientation of the lanes.

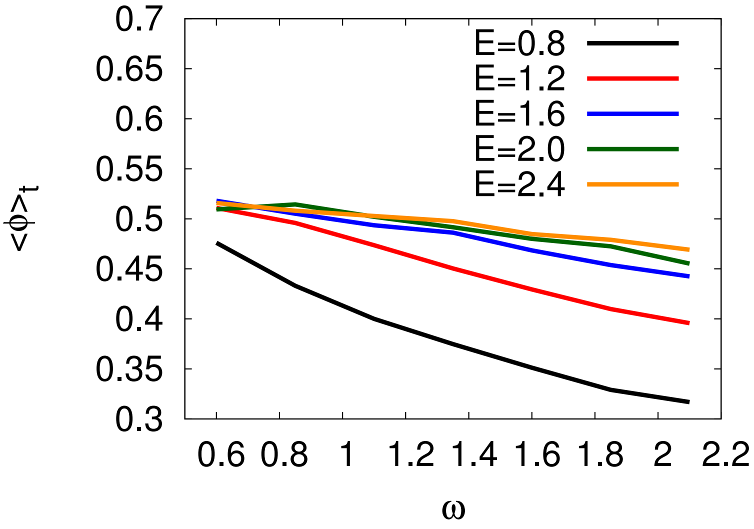

FIGURE 7.9: Time average of the segregation parameter.

7.1.1 Voronoi tessellation analysis

Voronoi tessellation is a method that divides the system into cells containing only one particle. The condition to draw a Voronoi diagram is that the closest particle to any point inside the cell has to be the particle in its interior. This way, the system is subdivided into N cells that cover all area. The edges of the cells are the segments that bisects the straight line connecting two closest neighbors and its vertices are the points at which these bisectors meet.

The advantage of using this method is that even though we have a continuous system it becomes possible to identify each particle closest neighbors (two neighboring particles

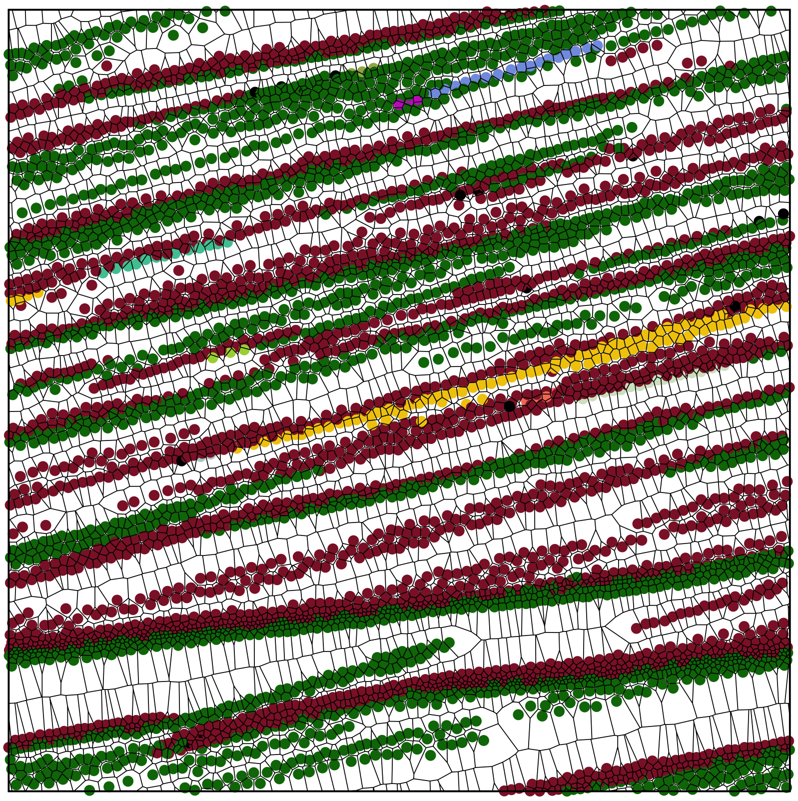

FIGURE 7.10: Voronoi tessellation of the system at a given time. The colors represent different clusters. Black particles are isolated and do not belong to any cluster. The black lines show the limits of the Voronoi cells. We can see that the area of the cells depends on the position the their particles occupy inside a lane.

are inside cells that share an edge). After the complete neighbor list is done, we can find the clusters of type A and B.

We use the Fortune's algorithm to draw the Voronoi diagram [61]. To identify the clusters we wrote a clustering function that reads the neighbor list in a recursive way (it scans all the neighbors linked by the list) and adds a particle to a burning list the first time it is found and grouped in a cluster. This way, the function does not consider the particle the next times it is found in the neighbor list.

In Fig. 7.6 we show the evolution of the number of clusters for the second time period of the system from Fig. 7.6 with $\omega = 0.6$ and $E = 2$, which is already in the stationary state. When the shift increases the number of clusters decreases. These times correspond to a lane configuration in which a system is composed by only a few clusters. During the times of rearrangement, the shift is low and the number of clusters is a high value that changes rapidly, which confirms that the system crosses a state of disorder after the breakage of the interfaces.

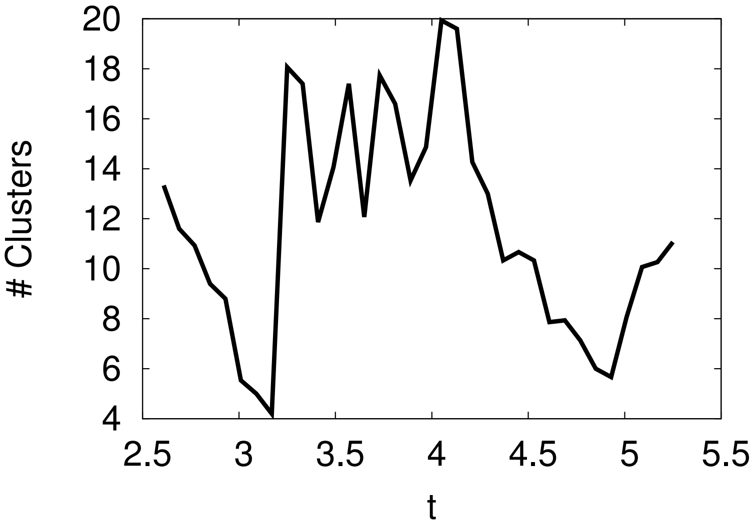

FIGURE 7.11: Number of clusters during the second time period of the system from Fig. 7.6 with $\omega = 0.6$ and $E = 2$. This result is the average of fifteen samples.

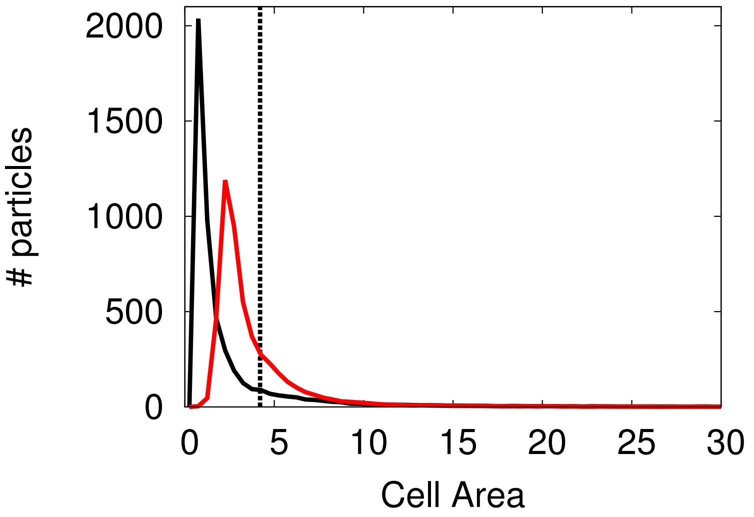

FIGURE 7.12: Distribution of the area of the cells for $t = 3.17$ (in black) and $t = 4.05$ (in red) of the system from Fig. 7.6 with $\omega = 0.6$ and $E = 2$. The vertical dashed line marks the area of the cells if the particles were uniformly distributed in space.

The cells in Figure 7.10 indicate that their area depend on the position of the particle inside the lane. Particles near an interface have a smaller cell than the ones on the opposite side, which results from the greater density of particles in these regions. In Figure 7.12 we show the distribution of the cell's area of the previous system at two different times. The black line corresponds to a period of low number of clusters ($t = 3.17$) and the red line to a period of high number of clusters ($t = 4.05$). It shows that in fact the distribution changes with the degree of order of the system. The peak of the distribution appears for smaller areas in the ordered state (in black), indicating the existence of regions with high density, while in the disordered state the peak is wider and closer to the area of the system divided by the number of particles that is marked by the vertical line.

The analysis of the number of clusters, cell area distribution and shift θ proved to be useful for identifying the states of the system. In conjugation with the magic angle formula (Eq. 7.2) we can also determine the lanes orientation at a given time.

Chapter 8

Conclusions

We first studied the dependence of the structure and relaxation dynamics of the equilibrium state of a colloidal suspension on the external potential and the interpaticle interaction. The analysis based on density-functional theory was found to be in good agreement with the results from Brownian dynamics simulations.

In the stationary state the system exhibits a band-like structure. The thickness of the bands measured in terms of the mean square displacement, σ, decreases with the strength of the potential, which leads in turn to higher densities around the external potential minima. We also showed that σ scales as P^{-2}, where P is the number of bands. In the limit of weak external potentials, σ increases linearly with the potential strength, V_E.

The relaxation towards the stationary extreme densities is exponential but the relaxation times are different. The system takes longer to reach equilibrium at the density maxima except when the external potential becomes significant weak in which case the relaxation time does not depend on the position. At the density maxima τ^{relax} decreases when both V_E and A increase but at the density minima it displays a more complex behavior and there is a maximum relaxation time that depends on the balance between V_E and A.

Electromagnetic fields are used in the laboratory to promote the formation of a variety of colloidal structures. These results quantify the relaxation times and the equilibrium structures of simple colloidal systems, which exhibit a rich behaviour that may be controlled in a straightforward manner.

The second study involved formation and destruction of lanes under a rotating external field. We found that lanes form obstacles that prevent opposite charged particles to move according with the direction of the field, resulting in resilience to small rotations. However, the interfaces between opposite charged lanes cannot withstand the constant change of the field direction, they break eventually and the system goes into a disordered state. The counterflow induces the creation of lanes in new orientations that, in a system with periodic boundary conditions, are quantized and follow the magic angles Ψ, which depend on the geometry of the system only. Lanes orientation is imposed by the magic angle closer to the angle of the field at the moment of rearrangement.

For low angular velocity ω, the lane orientation and approximate time of formation can be determined by the parameters of the field. In this regime the evolutions of several samples are very consistent and they become periodic with the periodicity of the magic angles. The initial conditions only affect the first period after which the system enters the stationary state. For high ω, the behavior is not so simple to describe. Lanes are formed at irregular times but their orientation still follows the magic angles.

We also studied the average of the shift between the direction of the field and the average particle velocities θ in the stationary state as function of the parameters. We showed that the shift increases with ω and decreases with E. We introduced the parameter ϕ that measures the segregation of particles. Time periods of stable lane configurations coincide with high segregation. The average segregation in the stationary state decreases with ω and increases with E. Increasing angular velocities promotes mixed states with the average particle trajectories increasingly shifted from the fields direction. Increasing the intensity of the field leads to the opposite effect.

Finally, we made a Voronoi tessellation to identify the clusters and estimate the area of each cell. When lanes are formed the system has only two clusters (one lane of each type), which is also a consequence of using periodic boundary conditions. In periods of mixing the number of clusters can increase ten fold and it rapidly oscillates, the clusters are highly dynamic structures during these periods. The cell area distribution also has distinctive features in both states. Most of the cells are smaller than the average area per particle in both cases but in a lane configuration state cells the peak of the distribution is more prominent and for smaller areas. In this state cells near the interface are very small, which is a consequence of the compression, while away from the interface cell areas can be of several particle sizes.

We found that the time at which lanes are formed and their orientation in a colloidal system subjected to a rotational external field can be determined with the parameters of the field.

We finish this thesis with some comments on possible directions of future studies. In the band system it would be interesting to study how the introduction of different particle species changes the band structure. Particles of distinct sizes also have different diffusivity and friction coefficients. The structures should be affected not only by the size asymmetry but also by their different dynamics. Another interesting case is to study how the bands behave when we force them to move in the direction perpendicular to their orientation. Do bands endure the effect of particles entering and moving away from high density regions? If not, how are they deformed?

In the lane system it would be useful to find the parameter region in which the system has a highly predictable behavior, i.e., when lanes orientation and formation times are determined by the field parameters. Also, the study the of lanes resilience can still be pushed further. We believe there is a relationship between lane stability and the particles velocity at the interface. Increasing the tangential collisions intensity in these regions should increase the stability. It would also be interesting to find the maximum compression that the interfaces can hold using the Voronoi cells area.

Bibliography

[1] M. H. Lash, M. V. Fedorchak, J. J. McCarthy, and S. R. Little. Scaling up self-assembly: bottom-up approaches to macroscopic particle organization. *Soft Matter*, 11:5597–5609, 2015. doi: 10.1039/C5SM00764J.

[2] Alfons van Blaaderen and Pierre Wiltzius. Real-space structure of colloidal hard-sphere glasses. *Science*, 270(5239):1177–1179, 1995. doi: 10.1126/science.270.5239.1177.

[3] Alfons van Blaaderen. Materials science: Colloids get complex. *Nature*, 439:545–546, 2006. ISSN 0028-0836. doi: 10.1038/439545a.

[4] Shin-Hyun Kim, Su Yeon Lee, and Seung-Man Yang. Self-assembled colloidal structures for photonics. *NPG Asia Mater*, 3:25–33, 2011. doi: 10.1038/asiamat.2010.192.

[5] P. F. Damasceno, M. Engel, and S. C. Glotzer. Predictive self-assembly of polyhedra into complex structures. *Science*, 337:453, 2012.

[6] Stefano Sacanna, David J. Pine, and Gi-Ra Yi. Engineering shape: the novel geometries of colloidal self-assembly. *Soft Matter*, 9:8096–8106, 2013. doi: 10.1039/C3SM50500F.

[7] Cristóvão S. Dias, Nuno A. M. Araújo, and Margarida M. Telo da Gama. Non-equilibrium adsorption of 2anb patchy colloids on substrates. *Soft Matter*, 9:5616–5623, 2013. doi: 10.1039/C3SM50386K.

[8] Nienke Geerts and Erika Eiser. Dna-functionalized colloids: Physical properties and applications. *Soft Matter*, 6:4647–4660, 2010. doi: 10.1039/C001603A.

[9] A Cadilhe, N A M Araújo, and Vladimir Privman. Random sequential adsorption: from continuum to lattice and pre-patterned substrates. *Journal of Physics: Condensed Matter*, 19(6):065124, 2007.

[10] N. A. M. Araújo, A. Cadilhe, and Vladimir Privman. Morphology of fine-particle monolayers deposited on nanopatterned substrates. *Phys. Rev. E*, 77:031603, Mar 2008. doi: 10.1103/PhysRevE.77.031603.

[11] Valeria Garbin. Colloidal particles: Surfactants with a difference. *Phys. Today*, 66 (10):68, 2013.

[12] C. S. Dias, N. A. M. Araújo, and M. M. Telo da Gama. Nonequilibrium growth of patchy-colloid networks on substrates. *Phys. Rev. E*, 87:032308, Mar 2013. doi: 10.1103/PhysRevE.87.032308.

[13] Ludovico Cademartiri and Kyle J. M. Bishop. Programmable self-assembly. *Nat Mater*, 14:2–9, 2015.

[14] N A M Araújo, C S Dias, and M M Telo da Gama. Kinetic interfaces of patchy particles. *Journal of Physics: Condensed Matter*, 27(19):194123, 2015.

[15] Nuno M. Silvestre, Qingkun Liu, Bohdan Senyuk, Ivan I. Smalyukh, and Mykola Tasinkevych. Towards template-assisted assembly of nematic colloids. *Phys. Rev. Lett.*, 112:225501, Jun 2014. doi: 10.1103/PhysRevLett.112.225501.

[16] Tarlan A. Vezirov, Sascha Gerloff, and Sabine H. L. Klapp. Manipulating shear-induced non-equilibrium transitions in colloidal films by feedback control. *Soft Matter*, 11:406–413, 2015. doi: 10.1039/C4SM01414F.

[17] James W. Swan, Jonathan L. Bauer, Yifei Liu, and Eric M. Furst. Directed colloidal self-assembly in toggled magnetic fields. *Soft Matter*, 10:1102–1109, 2014. doi: 10.1039/C3SM52663A.

[18] James W. Swan, Jonathan L. Bauer, Yifei Liu, and Eric M. Furst. Directed colloidal self-assembly in toggled magnetic fields. *Soft Matter*, 10:1102–1109, 2014. doi: 10.1039/C3SM52663A.

[19] Stefanie M. Cattes, Sabine H. L. Klapp, and Martin Schoen. Condensation, demixing, and orientational ordering of magnetic colloidal suspensions. *Phys. Rev. E*, 91: 052127, May 2015. doi: 10.1103/PhysRevE.91.052127.

[20] H. Löwen. Introduction to colloidal dispersions in external fields. *The European Physical Journal Special Topics*, 222(11):2727–2737, 2013. ISSN 1951-6355. doi: 10.1140/epjst/e2013-02054-3.

[21] Jure Dobnikar, Alexey Snezhko, and Anand Yethiraj. Emergent colloidal dynamics in electromagnetic fields. *Soft Matter*, 9:3693–3704, 2013. doi: 10.1039/C3SM27363F.

[22] Gary B. Davies, Timm Krüger, Peter V. Coveney, Jens Harting, and Fernando Bresme. Assembling ellipsoidal particles at fluid interfaces using switchable dipolar capillary interactions. *Advanced Materials*, 26(39):6715–6719, 2014. doi: 10.1002/adma.201402419.

[23] Patrick Dillmann, Georg Maret, and Peter Keim. Two-dimensional colloidal systems in time-dependent magnetic fields. *The European Physical Journal Special Topics*, 222(11):2941–2959, 2013. ISSN 1951-6355. doi: 10.1140/epjst/e2013-02068-9.

[24] Ahmet F. Demirörs, Pramod P. Pillai, Bartlomiej Kowalczyk, and Bartosz A. Grzybowski. Colloidal assembly directed by virtual magnetic moulds. *Nature*, 503: 99–103, 2013. doi: 10.1038/nature12591.

[25] F. Evers, R.D.L. Hanes, C. Zunke, R.F. Capellmann, J. Bewerunge, C. Dalle-Ferrier, M.C. Jenkins, I. Ladadwa, A. Heuer, R. Castañeda Priego, and S.U. Egelhaaf. Colloids in light fields: Particle dynamics in random and periodic energy landscapes. *The European Physical Journal Special Topics*, 222(11):2995–3009, 2013. ISSN 1951-6355. doi: 10.1140/epjst/e2013-02071-2.

[26] Randall M. Erb, Hui S. Son, Bappaditya Samanta, Vincent M. Rotello, and Benjamin B. Yellen. Magnetic assembly of colloidal superstructures with multipole symmetry. *Nature*, 457:999–1002, 2009. doi: 10.1038/nature07766.

[27] J. Yan, S. C. Bae, and S. Granick. Rotating crystals of magnetic janus colloids. *Soft Matter*, 11:147–153, 2015. doi: 10.1039/C4SM01962H.

[28] Sebastian Jäger, Heiko Schmidle, and Sabine H. L. Klapp. Nonequilibrium condensation and coarsening of field-driven dipolar colloids. *Phys. Rev. E*, 86:011402, Jul 2012. doi: 10.1103/PhysRevE.86.011402.

[29] Sebastian Jager and Sabine H. L. Klapp. Pattern formation of dipolar colloids in rotating fields: layering and synchronization. *Soft Matter*, 7:6606–6616, 2011. doi: 10.1039/C1SM05343D.

[30] James E Martin and Alexey Snezhko. Driving self-assembly and emergent dynamics in colloidal suspensions by time-dependent magnetic fields. *Reports on Progress in Physics*, 76(12):126601, 2013.

[31] K.R. Sütterlin, H.M. Thomas, A.V. Ivlev, G.E. Morfill, Vladimir E. Fortov, A.M. Lipaev, V.I. Molotkov, O.F. Petrov, A. Wysocki, and H. Löwen. Lane formation in driven binary complex plasmas on the international space station. *Plasma Science, IEEE Transactions*, 38:861 – 868, 2009.

[32] C-R Du, K R Sütterlin, K Jiang, C Räth, A V Ivlev, S Khrapak, M Schwabe, H M Thomas, V E Fortov, A M Lipaev, V I Molotkov, O F Petrov, Y Malentschenko, F Yurtschichin, Y Lonchakov, and G E Morfill. Experimental investigation on lane formation in complex plasmas under microgravity conditions. *New Journal of Physics*, 14(7):073058, 2012.

[33] Dirk Helbing, Lubos Buzna, Anders Johansson, and Torsten Werner. Self-organized pedestrian crowd dynamics: Experiments, simulations, and design solutions. *Transportation Science*, 39(1):1–24, 2005. doi: 10.1287/trsc.1040.0108.

[34] Moussaid M, Guillot EG, Moreau M, Fehrenbach J, Chabiron O, and et al. Lemercier S. Traffic instabilities in self-organized pedestrian crowds. *PLoS Comput Biol*, 8(3), 2012. doi: 10.1371/journal.pcbi.1002442.

[35] Teun Vissers, Adam Wysocki, Martin Rex, Hartmut Lowen, C. Patrick Royall, Arnout Imhof, and Alfons van Blaaderen. Lane formation in driven mixtures of oppositely charged colloids. *Soft Matter*, 7:2352–2356, 2011. doi: 10.1039/C0SM01343A.

[36] J. Dzubiella, G. P. Hoffmann, and H. Löwen. Lane formation in colloidal mixtures driven by an external field. *Phys. Rev. E*, 65:021402, Jan 2002. doi: 10.1103/PhysRevE.65.021402.

[37] J. Chakrabarti, J. Dzubiella, and H. Löwen. Reentrance effect in the lane formation of driven colloids. *Phys. Rev. E*, 70:012401, Jul 2004. doi: 10.1103/PhysRevE.70.012401.

[38] B. J. Alder, D. M. Ceperley, and E. L. Pollock. Computer simulation of phase transitions in classical and quantum systems. *International Journal of Quantum Chemistry*, 22(S16):49–61, 1982. doi: 10.1002/qua.560220808.

[39] C Vega, E Sanz, J L F Abascal, and E G Noya. Determination of phase diagrams via computer simulation: methodology and applications to water, electrolytes and proteins. *Journal of Physics: Condensed Matter*, 20(15):153101, 2008.

[40] J. Q. Broughton and X. P. Li. Phase diagram of silicon by molecular dynamics. *Phys. Rev. B*, 35:9120–9127, Jun 1987. doi: 10.1103/PhysRevB.35.9120.

[41] M. P. Allen and D. J. Tildesley. *Computer Simulation of Liquids.* Clarendon Press, 1989. ISBN 0-19-855645-4.

[42] F.A. Bettelheim, W.H. Brown, M.K. Campbell, and S.O. Farrel. *Introduction to General, Organic and Biochesmestry.* Mary Finch, 2010.

[43] B. Derjaguin and L. Landau. Theory of the stability of strongly charged lyophobic sols and of the adhesion of strongly charged particles in solutions of electrolytes. *Acta Physico Chemica URSS*, 14, 1941.

[44] E. J. W. Verwey and J. Th. G. Overbeek. *Theory of the stability of lyophobic colloids.* Elsevier, 1948.

[45] A. Satoh. *Introduction to Practice of Molecular Simulation: Molecular Dynamics, Monte Carlo, Brownian Dynamics, Lattice Boltzmann and Dissipative Particle Dynamics.* Elsevier Insights, 2010.

[46] G. K. Batchelor. *An Introduction to Fluid Dynamics.* Cambridge University Press, 2000.

[47] H. Risken. *The Fokker-Planck Equation. Methods of Solution and Applications.* Springer-Verlag, 1996.

[48] A. Einstein. Un the movement of small particles suspended in stationary liquids required by the molecular-kinetic theory of heat. *Ann. der Physik*, 17, 1905.

[49] D. Frenkel. *Understanding Molecular Simulation. From Algorithms to Applications.* Academic Press, 2001.

[50] D. C. Rapaport. *The Art of Molecular Dynamics Simulation.* Cambridge University Press, 2004.

[51] A. C. Brańka and D. M. Heyes. Algorithms for brownian dynamics computer simulations: Multivariable case. *Phys. Rev. E*, 60:2381–2387, Aug 1999.

[52] boost/random/mersenne_twister.hpp from the boost c++ libraries.

[53] M. Matsumoto and T. Nishimura. Mersenne twister: a 623-dimensionally equidistributed uniform pseudo-random number generator. *ACM Transactions on Modeling and Computer Simulation*, 8:3–30, 1998. doi: 10.1145/272991.272995.

[54] G. E. P. Box and M. E. Muller. A note on the generation of random normal deviates. *The Annals of Mathematical Statistics*, 29:610–611, 1958.

[55] Umberto Marini Bettolo Marconi and Pedro Tarazona. Dynamic density functional theory of fluids. *The Journal of Chemical Physics*, 110(16):8032–8044, 1999. doi: http://dx.doi.org/10.1063/1.478705.

[56] M Rauscher. Ddft for brownian particles and hydrodynamics. *Journal of Physics: Condensed Matter*, 22(36):364109, 2010.

[57] Stefano Zapperi, André A. Moreira, and José S. Andrade. Flux front penetration in disordered superconductors. *Phys. Rev. Lett.*, 86:3622–3625, Apr 2001. doi: 10.1103/PhysRevLett.86.3622.

[58] Petrucio Barrozo, André A. Moreira, J. Albino Aguiar, and José S. Andrade. Model of overdamped motion of interacting magnetic vortices through narrow superconducting channels. *Phys. Rev. B*, 80:104513, Sep 2009. doi: 10.1103/PhysRevB.80.104513.

[59] The COMSOL multiphysics software is used to implement the FEM.

[60] M. Rex and H. Löwen. Lane formation in oppositely charged colloids driven by an electric field: Chaining and two-dimensional crystallization. *Phys. Rev. E*, 75: 051402, May 2007. doi: 10.1103/PhysRevE.75.051402.

[61] S Fortune. A sweepline algorithm for voronoi diagrams. In *Proceedings of the Second Annual Symposium on Computational Geometry*, SCG '86, pages 313–322, New York, NY, USA, 1986. ACM. ISBN 0-89791-194-6. doi: 10.1145/10515.10549.